NMR DETECTION OF IONIZED ARSENIC VACANCY PRODUCTION IN GALLIUM ARSENIDE

A Dissertation

Presented to

The Faculty of the Department of Physics

The College of William and Mary in Virginia

In Partial Fulfillment

Of the Requirements for the Degree of

Doctor of Philosophy

---

by

Richard K. Hester

June 1974

APPROVAL SHEET

This dissertation is submitted in partial fulfillment of

the requirements for the degree of

Doctor of Philosophy

in

Physics

Richard K Hester
Author

Approved, April 1974

Jon F. Soest
Jon F. Soest, Ph.D.

Arden Sher
Arden Sher, Ph.D.

Irving A. Lowe
Irving A. Lowe, Ph.D.

Frederic R. Crownfield
Frederic R. Crownfield, Ph.D.

Kenneth G. Petzinger
Kenneth G. Petzinger, Ph.D.

NMR DETECTION OF IONIZED ARSENIC VACANCY PRODUCTION IN GALLIUM ARSENIDE

TABLE OF CONTENTS

LIST OF FIGURES

ABSTRACT

Pulsed NMR was used to detect charged defect concentrations as small as 2×10^{14} cm^{-3}. An undoped n-type single crystal of GaAs was cut into several samples, and NMR second moments were obtained as a function of magnetic field orientation for Ga^{71}, Ga^{69}, and As^{75}. The orientationally dependent part of the Ga^{71} second moment is one half that expected from the dipolar interaction. An explanation is given based on interference between the dipolar and the negative pseudodipolar interactions. There is a contribution to the second moment due to the electric quadrupole interaction between nuclei and the electric field gradient (efg) associated with point charge like defects, and it is proportional to the defect concentration. Because there are three isotopes we can separately identify the quadrupolar and pseudodipolar second moments, and the preferred defect location.

In order to introduce crystalline defects, samples were held at a constant temperature (500°C, 550°C, 600°C, 700°C) in evacuated tubes and quenched to room temperature. The increase in second moment is due to the increased quadrupolar contribution, and it establishes the defect density for each damaged sample. The pseudodipolar interaction is observed to be independent of damage. Our data indicate that the defects are located on the As nuclear sites, and no annealing was observed. We conclude that the defects are As monovacancies. An independent method

of estimating the defect density produced by a quench is discussed. The agreement between the predicted defect densities and our data is good.

I. INTRODUCTION

Technologically, GaAs is an important compound that is used in the construction of many modern electronic devices. The performance and lifetime of these devices can depend sensitively upon the crystalline defects. One particular type of defect that is thought to be important is the vacancy. Unexplained phenomena are often attributed to vacancies. However, unlike impurity atoms, their presence is difficult to detect, so their role in crystal properties is not well established.

Hall effect measurements can detect the net sign and density of the charge carriers in solids, and the carrier concentration is frequently equated with the crystal defect concentration. Vacancies that behave as donors or acceptors can be detected. However if donors and acceptors are present in identical concentrations, there will be no charge carriers. An undoped sample with a vanishing carrier concentration would be interpreted as a very pure crystal, but it might contain a large number of ionized defects.

NMR measurements can supplement carrier concentration measurements. The existence of a defect at a nuclear site will disturb the electronic charge distribution in the vicinity. It will cause a net change in the electric field, and thus the electric field gradient (efg) at nearby nuclear positions. Nuclei with quadrupole moments will interact with this efg, and since the NMR line is sensitive to small changes in nuclear energy

levels, one may use NMR to detect these crystalline defects in GaAs. Both donors and acceptors disturb the efg in their vicinities, and the NMR technique will detect the sum of their concentrations. However, the effect of this interaction on the NMR line must be identified in the presence of other nuclear interactions.

In III-V compounds, the broadening of the NMR line is due to four rigid lattice interactions. In particular, the second moments of the three isotopic species in GaAs (Ga^{71}, Ga^{69}, and As^{75}) contain contributions from all four of these mechanisms.

The dipolar interaction is well understood, and its contribution to the NMR second moment may be calculated theoretically.[1] In 1957 Schulman, et al.[2,3] reported linewidths in undoped powder samples of GaAs larger than those expected from the dipolar interaction alone. The additional broadening was attributed to the indirect exchange interaction between unlike spin systems. This nuclear exchange interaction involves an indirect nuclear spin coupling[4-6] via the hyperfine interaction between the electronic and nuclear spins. Its magnitude depends mainly upon the s character of the electronic wave function at the nuclear positions. More recently, Sundfors[7] has observed linewidths in several III-V compounds using both NMR and nuclear acoustic resonance (NAR) techniques. He identified the exchange contribution to the second moments and, using the theory of Anderson,[6] the exchange coupling constants.

Another electron coupled interaction is the pseudodipolar interaction.[4] The role of this mechanism in the broadening of NMR lines in III-V compounds is not well established, but a large negative pseudodipolar

effect (canceling some dipolar broadening) has been observed in P^{31} resonance in InP.[8] The pseudodipolar interaction will be required to explain the data reported here. In undamaged samples both the Ga^{69} and Ga^{71} NMR second moments are smaller than those predicted by the dipolar interaction alone. In this case, the sign of the pseudodipolar coupling constant may be unambiguously determined.

GaAs has a zinc blende structure. This may be described as two interpenetrating face-centered cubic sublattices, one containing Ga atoms, and the other As. These two sublattices are displaced by one quarter of the cubic body diagonal. Thus each atom is surrounded by a tetrahedron of four nearest neighbors on the other sublattice, and the efg at nuclear sites is zero unless there are lattice defects. Randomly located lattice defects cause a random efg at nuclear sites and broaden the NMR line.

E. H. Rhoderick[9] observed the effects of substitutional impurities upon NMR line intensities. The intensity loss with increasing impurity concentration is due to quadrupolar broadening caused by the efg associated with the impurities. It was found that the efg associated with ionized donor or acceptor impurities is larger than that associated with strains produced by neutral impurities. The explanation of the sensitivity of the NMR line to the ionized impurities[10] required anomalously large antishielding factors on the order of 1000.

Gill and Bloembergen[11] reported a direct measurement of the coupling constant relating the components of an efg tensor to an applied homogeneous electric field. The efg induced at nuclear sites is caused partly by a distortion of the valence orbitals and partly by a relative

displacement of the Ga and As sublattices. Taking both effects into account, the coupling constant was explained using antishielding factors of 24 and 30 for Ga and As, respectively. Since the induced efg is proportional to the electric field, its magnitude decreases as r^{-2} in the field of a point charge. In contrast, the direct efg caused by a point charge decreases as r^{-3}. Thus the quadrupolar interaction is dominated by the induced efg. Using this induced quadrupolar interaction it is not necessary to introduce large antishielding factors to explain Rhoderick's data.

Sundfors[7] identified the electric quadrupolar contribution to the NAR linewidths in samples of known carrier concentration. Comparing his measured linewidths to those predicted by a simplified theory of the induced quadrupole interaction linewidth, in which the number of charge centers is set equal to the carrier concentration, he obtained order of magnitude agreement with the measurements of Gill and Bloembergen.

In this research it is demonstrated that NMR linewidths can be used to measure low concentrations of charged defects in single crystals of GaAs. This is done with careful measurements of NMR second moments as a function of magnetic field orientation for all three isotopic species. Individual contributions from the four broadening interactions are identified; and, using an improved efg model, it is shown that the first order quadrupolar contribution is proportional to the charged defect concentration. Thus this concentration can be measured by the quadrupolar contribution to the second moment.

Defect concentrations in several samples are altered by subjecting the samples to thermal damage. The process is similar to that of Potts

and Pearson,[12] but these damage temperatures are far lower, producing fewer defects (on the order of 2×10^{14} cm^{-3}, compared to their 10^{18} cm^{-3}). With increasing damage, an increase in the quadrupolar contribution to the second moment is observed. The charged defect density measured agrees with a thermodynamic calculation of the density of charged As monovacancies that one expects to be produced.

A report of this experiment follows. In the next section, the theoretical second moment expression for the GaAs lattice is evaluated. Then the experimental details are given in Section III. The analysis of the experimental data is described in Section IV. Finally, a discussion of the results and a summary are given in Sections V and VI.

II. THEORY

Consider two different nuclear-spin systems with nuclei having spin angular momentum $\hbar\vec{I}$ and $\hbar\vec{S}$, and non-overlapping resonances. The resonance experiment is performed on the spins I. We assume that the resonance is broadened by the following four interactions: dipolar, pseudodipolar, exchange, and quadrupolar. The second moment of the resonance line is calculated from the expression given by van Vleck[1]

$$\langle \Delta H^2 \rangle = \gamma_I^{-2} \hbar^{-2} \frac{\mathrm{Tr}[\mathcal{H}, \hat{I}]^2}{\mathrm{Tr}[\hat{I}^2]} , \tag{1}$$

where $\mathcal{H}$ is the system hamiltonian, and $\hat{I}$ is the total spin operator proportional to the observed magnetization.

Following the notation of Sundfors,[7] we write the system hamiltonian as

$$\mathcal{H} = \mathcal{H}_{0I} + \mathcal{H}_{0S} + \mathcal{H}_{DI} + \mathcal{H}_{DS} + \mathcal{H}_{DIS} + \mathcal{H}_{EI} + \mathcal{H}_{ES} + \mathcal{H}_{EIS} + \mathcal{H}_{PI} + \mathcal{H}_{PS} + \mathcal{H}_{PIS} + \mathcal{H}_{QI}, \tag{2}$$

where $\mathcal{H}_{0I}$ and $\mathcal{H}_{0S}$ are the Zeeman energies for the I and S spins, respectively. We may combine the truncated dipolar and pseudodipolar interaction[13] terms as

$$\mathcal{H}_{DI} + \mathcal{H}_{PI} = \gamma_I^2 \hbar^2 \sum_{i>j} (1 + B_{ij})(3 I_{iz} I_{jz} - \vec{I}_i \cdot \vec{I}_j) P_2(\theta_{ij}) r_{ij}^{-3}, \tag{3a}$$

$$\mathcal{H}_{DS}+\mathcal{H}_{PS}=\gamma_S^2\hbar^2\sum_{i>j}(1+\tilde{B}'_{ij})(3S_{iz}S_{jz}-\vec{S}_i\vec{S}_j)P_2(\theta_{ij})r_{ij}^{-3}, \quad (3b)$$

$$\mathcal{H}_{DIS}+\mathcal{H}_{PIS}=\gamma_I\gamma_S\hbar^2\sum_{i,j}(1+\tilde{B}_{ij})I_{iz}S_{jz}P_2(\theta_{ij})r_{ij}^{-3}, \quad (3c)$$

where B_{ij} is the pseudodipolar coupling constant for like spins I, $\tilde{B}'_{ij}$ is the pseudodipolar coupling constant for like spins S, $\tilde{B}_{ij}$ is the pseudodipolar coupling constant for unlike spins I and S, and $\vec{r}_{ij}$ is the displacement vector from the i^{th} nuclear site. The second Legendre polynomial is written as $P_2(\theta_{ij})$, where θ_{ij} is the angle between and the Zeeman field. The exchange terms may be written

$$\mathcal{H}_{EI}=\sum_{i>j}A_{ij}\vec{I}_i\cdot\vec{I}_j, \quad (3d)$$

$$\mathcal{H}_{ES}=\sum_{i>j}\tilde{A}'_{ij}\vec{S}_i\cdot\vec{S}_j, \quad (3e)$$

$$\mathcal{H}_{EIS}=\sum_{i,j}\tilde{A}_{ij}I_{iz}S_{jz}, \quad (3f)$$

where A_{ij} is the exchange coupling constant for like spins I, $\tilde{A}'_{ij}$ is the exchange coupling constant for like spins S, and $\tilde{A}_{ij}$ is the exchange coupling constant for unlike spins I and S. The quadrupolar term can be written

$$\mathcal{H}_{QI}=A\sum_j(3I_{jz}^2-I_j^2)V_{zzj}, \quad (3g)$$

where V_{zz_j} is the efg at nuclear site j, and $A = eQ_I[4I(2I-1)]^{-1}$, where Q_I is the electric quadrupole moment of the spins I.

By combining Eqs. (1), (2), and (3), and neglecting the Zeeman terms in $\mathcal{H}$, one obtains the expression for the NMR second moment

$$\begin{aligned}\langle \Delta H^2 \rangle = {} & 3I(I+1)\gamma_I^2\hbar^2 \sum_j \left[(1+B_{ij}) r_{ij}^{-3} P_2(\theta_{ij})\right]^2 + \\ & + \tfrac{4}{3} S(S+1)\gamma_S^2\hbar^2 \sum_j \left[(1+\tilde{B}_{ij}) r_{ij}^{-3} P_2(\theta_{ij})\right]^2 + \\ & + \tfrac{9}{5}\left[4I(I+1)-3\right] A^2 N^{-1} \gamma_I^{-2}\hbar^{-2} \sum_j V_{zz_j}^2 + \\ & + \tfrac{1}{3} S(S+1) \sum_j \tilde{A}_{ij}^2 \,. \end{aligned} \tag{4}$$

Because the Zeeman terms have been neglected, this is the expression for the second moment about the center frequency of the resonance line.

The lattice sums in the dipolar and pseudodipolar terms of Eq. (4) may be separated into two parts, one of which contains no pseudodipolar coupling constants. Consider just that sum for like spin broadening. This may be written

$$\sum_j \left[(1+B_{ij}) r_{ij}^{-3} P_2(\theta_{ij})\right]^2 = \sum_j B_{ij}(2+B_{ij})\, r_{ij}^{-6} P_2^2(\theta_{ij}) + \sum_j r_{ij}^{-6} P_2^2(\theta_{ij}) \,. \tag{5}$$

The first sum on the right side of Eq. (5) contains the pseudodipolar contribution to the second moment and the interference term between the dipolar and pseudodipolar interactions. The second sum is just the dipolar contribution in the presence of zero pseudodipolar interactions. This sum

may be performed, and for the zinc blende lattice it has the form[1]

$$\sum_j r_{ij}^{-6} P_2^2(\theta_{ij}) = \frac{1}{8}\left[a + b(n_x^2 + n_y^2 + n_z^2)\right], \tag{6}$$

where n_x, n_y, and n_z are the direction cosines of the Zeeman field in the crystalline coordinate system. When the sum is performed over nuclear sites on the fcc sublattice containing the spins I, Sundfors computes $a = 256\ a_0^{-6}$ and $b = -118\ a_0^{-6}$, where a_0 is the lattice constant. For the non-resonant sublattice he computes $a' = 2491\ a_0^{-6}$ and $b' = -2390\ a_0^{-6}$.

If the magnetic field is rotated in the $(1\bar{1}0)$ plane, and Θ is defined as the angle between the [110] direction and the Zeeman field, then

$$n_x^4 + n_y^4 + n_z^4 = 1 - f(\Theta), \tag{7}$$

where $f(\Theta) = 2\cos^2\Theta - \frac{3}{2}\cos^4\Theta$. Combining Eqs. (6) and (7) we may write the dipolar sum in terms of $f(\Theta)$,

$$\sum_j r_{ij}^{-6} P_2^2(\theta_{ij}) = X + Y f(\theta), \tag{8}$$

where $X = (a + b)/8$, and $Y = -b/8$. The dipolar contribution to the NMR second moment thus contains an isotropic part, X, and a part dependent upon the magnetic field direction, Y.

We consider now the first sum on the right hand side of Eq. (5). The electron coupled pseudodipolar interaction is extremely short range,[5] and we assume that only nearest neighbors interact. Thus the first sum in Eq. (5) vanishes because a sum over like spins does not contain the

nearest neighbor shell. However, the corresponding term in the expression for unlike dipolar and pseudodipolar broadening does contain the nearest neighbor shell. The coefficients $\tilde{B}_{ij}$ are independent of θ_{ij} and may be factored out of the sum. The pseudodipolar terms become

$$\hbar^2\gamma_S^2 \sum_j \tilde{B}_{ij}(2+\tilde{B}_{ij}) r_{ij}^{-6} P_2^2(\theta_{ij}) = 2\hbar^2\gamma_S^2 \tilde{B}_{NN}(2+\tilde{B}_{NN})(4/a_0\sqrt{3})^6 f(\theta), \quad (9)$$

where $\tilde{B}_{NN}$ is the nearest neighbor pseudodipolar coupling constant. With this nearest neighbor approximation, the pseudodipolar terms have the same orientation dependence as the angular part of the dipolar contribution to the second moment, but there is no isotropic pseudodipolar contribution.

In order to evaluate the quadrupolar contribution to the second moment we require a specific model for the efg tensor. The efg associated with crystalline strain is much smaller than that caused by charged impurities[7,9] and may be neglected when both are present. Thus we assume that the efg is due entirely to the electric field of charged crystalline defects. The general tensor relationship between the components V_{ij} of the efg tensor and the applied electric field components E_k is given by[11,14]

$$V_{ij} = \sum_k R_{ijk} E_k , \quad (10)$$

where R is a third rank tensor. In the zinc blende crystalline coordinate system Eq. (10) may be written[15]

$$V = -R_{14} \begin{pmatrix} 0 & E_z & E_y \\ E_z & 0 & E_x \\ E_y & E_x & 0 \end{pmatrix}, \quad (11)$$

where R_{14} is the magnitude of the non-vanishing tensor components.

The component of V in the secular part of the quadrupole hamiltonian (that part which commutes with the Zeeman hamiltonian) is $\hat{n}\cdot V\cdot\hat{n}$, where $\hat{n}$ is the unit vector in the direction of the Zeeman field. We find

$$\hat{n}\cdot V\cdot\hat{n} = -2R_{14}(n_y n_z E_x + n_x n_z E_y + n_x n_y E_z). \tag{12}$$

Since most of the nuclei affected by a given impurity lie outside the first few near neighbor shells, we use the static macroscopic dielectric constant ϵ to approximate the electronic screening.[16] Thus the electric field at a displacement $\vec{r}$ from a single impurity of effective charge e* is

$$\vec{E} = e^*\vec{r}\,/\epsilon r^3. \tag{13}$$

Combining Eqs. (12) and (13) with the last term in Eq. (4), we obtain an expression for the quadrupolar contribution to the second moment for a single impurity

$$\langle\Delta H^2\rangle_{Q,1} = [4I(I+1)-3]\left(\frac{AR_{14}e^*}{\epsilon\gamma_I\hbar}\right)^2\frac{36}{5N}\sum r_{ij}^{-6}(n_y n_z x_j + n_x n_z y_j + n_x n_y z_j)^2. \tag{14}$$

Due to the lattice symmetry of GaAs, summations over terms $x_j y_j$, $x_j z_j$, and $y_j z_j$ vanish, and summations over terms x_j^2, y_j^2, and z_j^2 are equal. Using these and the properties of direction cosines we may rewrite Eq. (14)

$$\langle\Delta H^2\rangle_{Q,1} = \frac{6}{5}[4I(I+1)-3]\left(\frac{AR_{14}e^*}{\epsilon\gamma_I\hbar}\right)^2\frac{1}{N}\sum_j r_j^{-4} f(\theta). \tag{15}$$

We assume that N_I charged defects occur randomly on one sublattice. Each contributes to the second moment independently, so the quadrupolar second moment expression becomes

$$\langle \Delta H^2 \rangle_Q = \frac{6}{5}[4I(I+1)-3]\left(\frac{AR_{14}e^*}{\epsilon\gamma_I\hbar}\right)^2\left(\frac{\rho_I}{\rho}\right)f(\theta)\sum_j r_j^{-4} \qquad (16)$$

where the ratio of defect density to nuclear density ρ_I/ρ has replaced the ratio N_I/N. This contribution has the same angular dependence as the pseudodipolar second moment. Both vanish when $\theta = \frac{\pi}{2}$, where the Zeeman field is aligned with the [001] direction. The maximum quadrupolar broadening occurs at $\theta = \cos^{-1}(1/\sqrt{3})$, where the Zeeman field is aligned with the [111] direction.

We have calculated the lattice sum over r_j^{-4} in Eq. (16). The discrete sum was performed over a cube with an edge size of 16 a_0. An integral was performed over the remainder of the sample. The result of this calculation is 33.75 a_0^{-4} for impurities located on the same sublattice as the nuclear spins I, and 63.31 a_0^{-4} for the impurities located on the other sublattice. Thus, the average efg is different for nuclei on different sublattices if the defects have preferential sites. One may then use the experimental quadrupolar contributions to the second moment to determine the preferred defect sites.

II. EXPERIMENT

The free induction decay (FID) following a single 90° pulse was observed for each of the three nuclear isotopes as a function of magnetic field orientation. The NMR probe is cylindrical in shape, and it may be rotated in the magnetic field. The GaAs crystal was placed in the probe with its $[1\bar{1}0]$ axis parallel to the sample coil and the probe cylindrical axes. The probe was placed in the magnetic field with its rotation axis perpendicular to the lines of flux. In this way, a rotation of the probe can align the major crystal symmetry axes ([001], [110], and [111]) with the magnetic field.

Next, the [001] axis was aligned with the magnetic field using the FID as the alignment tool. With the magnetic field in the [001] direction, the FID does not cross the baseline, and the decay time is greater. The line shape is thus different from those at other orientations, and the alignment is easily attained. A comparison of the Ga^{69} FID in two orientations is shown in Fig. 1. The [001] orientation of the probe was given the angular designation 90°, corresponding to the angle θ defined in Eq. (7). A study of a given isotope consisted of the observation of its FID in 16 probe orientations ranging from -10° to 110°.

A thorough study of each isotope was made for each sample. Then, one at a time, the samples were thermally damaged. In the 24 hours following the damage, the As^{75} FID was observed in two magnetic field

Figure 1. Ga^{69} FID where H_0 is aligned with a) the [001] direction, and b) the [111] direction.

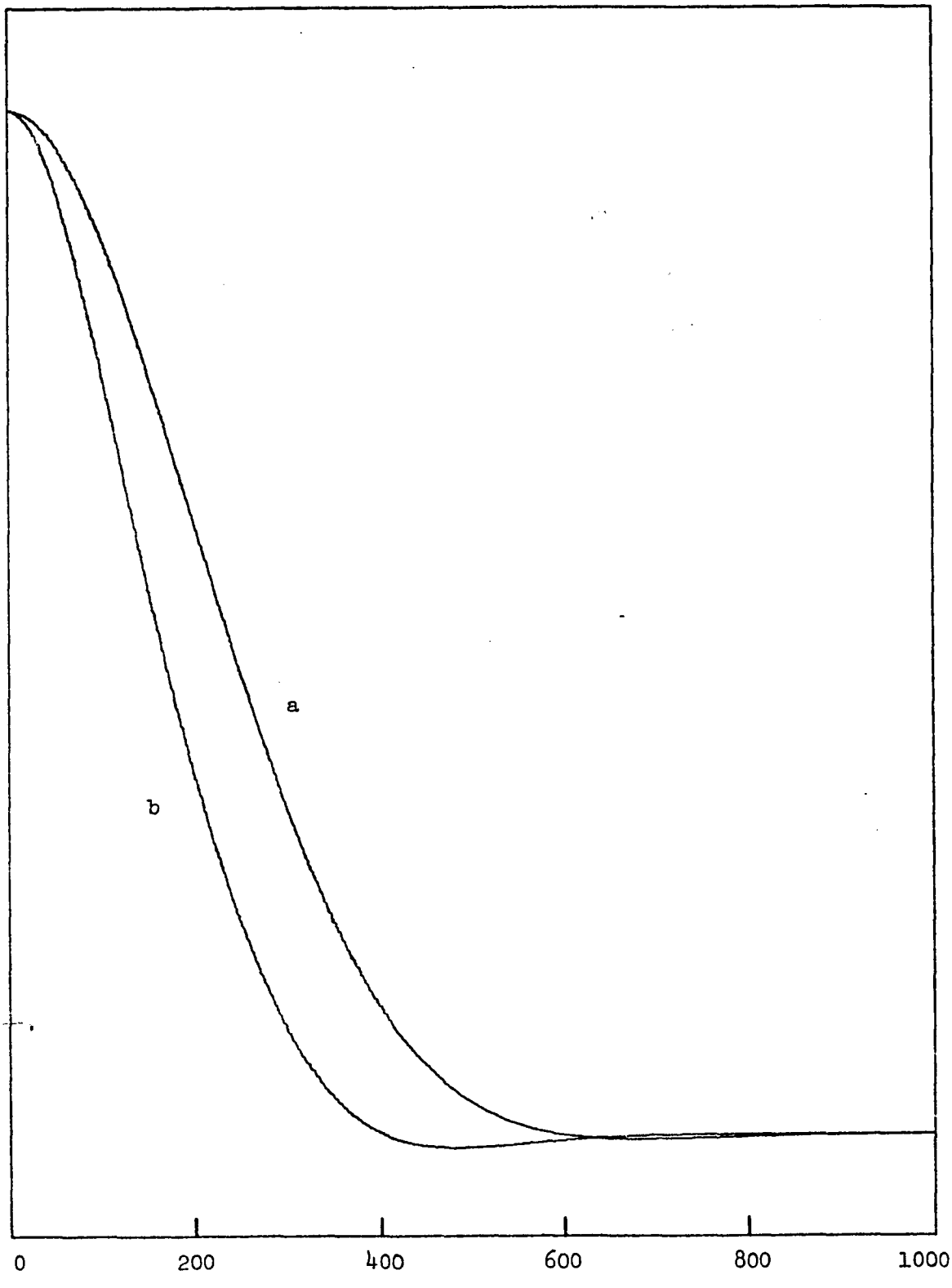
a
b
0
200
400
600
800
1000
TIME-MICROSECONDS

orientations as a function of time. The purpose of this procedure was to detect room temperature annealing of the damaged sample. The As^{75} FID was selected for this observation because, of the three isotopes, it has the shortest longitudinal relaxation time, T_1 (approximately .2 sec.). Thus the As^{75} FID could be signal averaged sufficiently in a shorter period of time, allowing more frequent sampling in the 24 hour period. Following this initial procedure, the magnetic field orientation study was repeated for each isotope.

A. Sample Preparation

The experiment was performed on several n-type single crystals of GaAs, sliced from a single undoped, boat grown ingot purchased from the Monsanto Company. The properties of the ingot were supplied by Monsanto as follows: resistivity, 2.7×10^3 ohm-cm; carrier concentration, 2.4×10^{11} cm^{-3}; electron mobility, 2.7×10^3 cm^2 $volt^{-1}$ sec^{-1}; and etch pit density, 4.2×10^4 cm^{-2}. A 50 micron diamond saw was used to cut the ingot into several samples of nearly equal size, about 0.5 cm by 0.5 cm by 1.0 cm.

In addition, an n-type silicon doped single crystal of GaAs was also studied. The purpose of this study was to compare the known carrier concentration with our measurement of defect density. The following properties were measured by the manufacturer, Electronic Materials Corporation: resistivity, 3×10^{-2} ohm-cm; carrier concentration, 4×10^{16} cm^{-3}; electron mobility, 5×10^3 cm^2 $volt^{-1}$ sec^{-1}; etch pit density, 8×10^4 cm^{-2}.

In order to produce a controlled vacancy concentration in the undoped samples, thermal damage was done using the method of Potts and

Pearson.[12,17] The sample was sealed in an evacuated vycor vessel. The pressure within the vessel was less than 10^{-3} Torr. This vessel was then placed in a cylindrical oven, and held at a constant elevated temperature for 24 hours after which it was quickly cooled. A separate thermocouple showed that the oven controller maintained the desired temperature within 5°C. The cooling took place when the sealed vessel was removed from the oven and left to stand in the room air. This quench thus occurs over a 10 to 15 minute period. A long quench period was used to avoid any macroscopic damage due to uneven cooling of the large crystals.

Ionic mobilities in GaAs at these temperatures are quite low,[18] so the vacancy concentration caused by sublimation of As or Schottky defects is not expected to depend upon the period of the quench. However, Frenkel pairs may recombine quickly, and the longer quench period used might substantially reduce their concentration.

B. Pulsed NMR Spectrometer

NMR measurements were made with a pulsed NMR system shown in block diagram form in Fig. 2. The master oscillator, rf gating and phasing, and phase detection are identical to those circuits described by Ellett, et al.[19] as spectrometer B.

The control of the experiment timing is provided by a pulse programmer designed and constructed in this laboratory. This pulse programmer is capable of generating a repetitive sequence of up to 16 steps in length, where either a pulse or a time delay separating pulses is considered a step. Further, it may be programmed to interrupt a given sequence

Figure 2. Block diagram of pulsed NMR spectrometer.

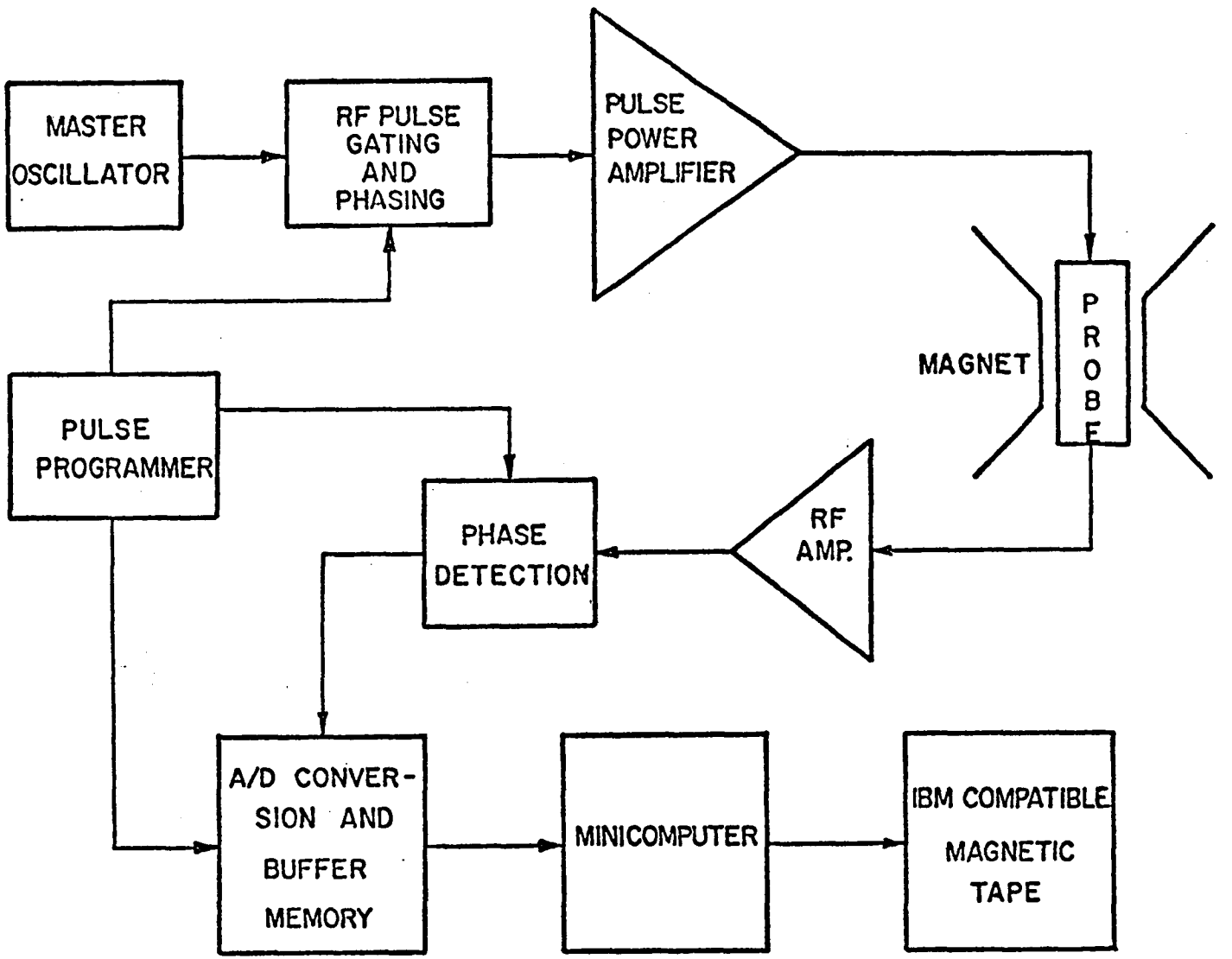
MASTER OSCILLATOR
RF PULSE GATING AND PHASING
PULSE POWER AMPLIFIER
MAGNET
PROBE
PULSE PROGRAMMER
PHASE DETECTION
RF AMP.
A/D CONVERSION AND BUFFER MEMORY
MINICOMPUTER
IBM COMPATIBLE MAGNETIC TAPE

after a specified number of steps by using either or both of two internal step counters. The combination of these features makes the programmer very versatile. Its design represents unreported work, so a rather detailed description is found in Appendix A.

The power amplifier was an NMR Specialties Model P-103R. It consists of two gated stages. The tube grids of each stage are normally held at -150 volts, keeping the tubes non-conducting. A grid gating pulse triggered by the pulse programmer raises this dc bias to 0 volts as the low level rf pulse is amplified. Amplification is damped quickly at the end of the pulse by returning the grids to -150 volts. In this experiment the power amplifier was broad-banded to yield 1.6 kilowatt pulses with 10% to 90% rise and fall times less than 1 microsecond at 14.5 MHz.

The rf preamplifier and signal duplexer are those designed by Lowe and Tarr,[20] modified for a 50 ohm system. The preamplifier consists of two stagger-tuned tube (7788) stages. There is no gating to protect it from pulse overdrive. The broad-band tuning allows a fast recovery. At 14.4 MHz the gain was $\sim$ 200 and the bandwidth was $\sim$ 1 MHz.

A cable exactly one quarter wavelength long has the property that the impedance of the cable with the far end shorted appears very large and resistive. It is this property that is used in the duplexer shown in Fig. 3. The quarter wavelength cable at the power amplifier does not affect the rf pulses, but serves to eliminate low frequency noise from the output of the power amplifier. The power amplifier drives a half wavelength cable that is terminated into a diode shunt at A. From there

Figure 3. Schematic of Signal Duplexing.

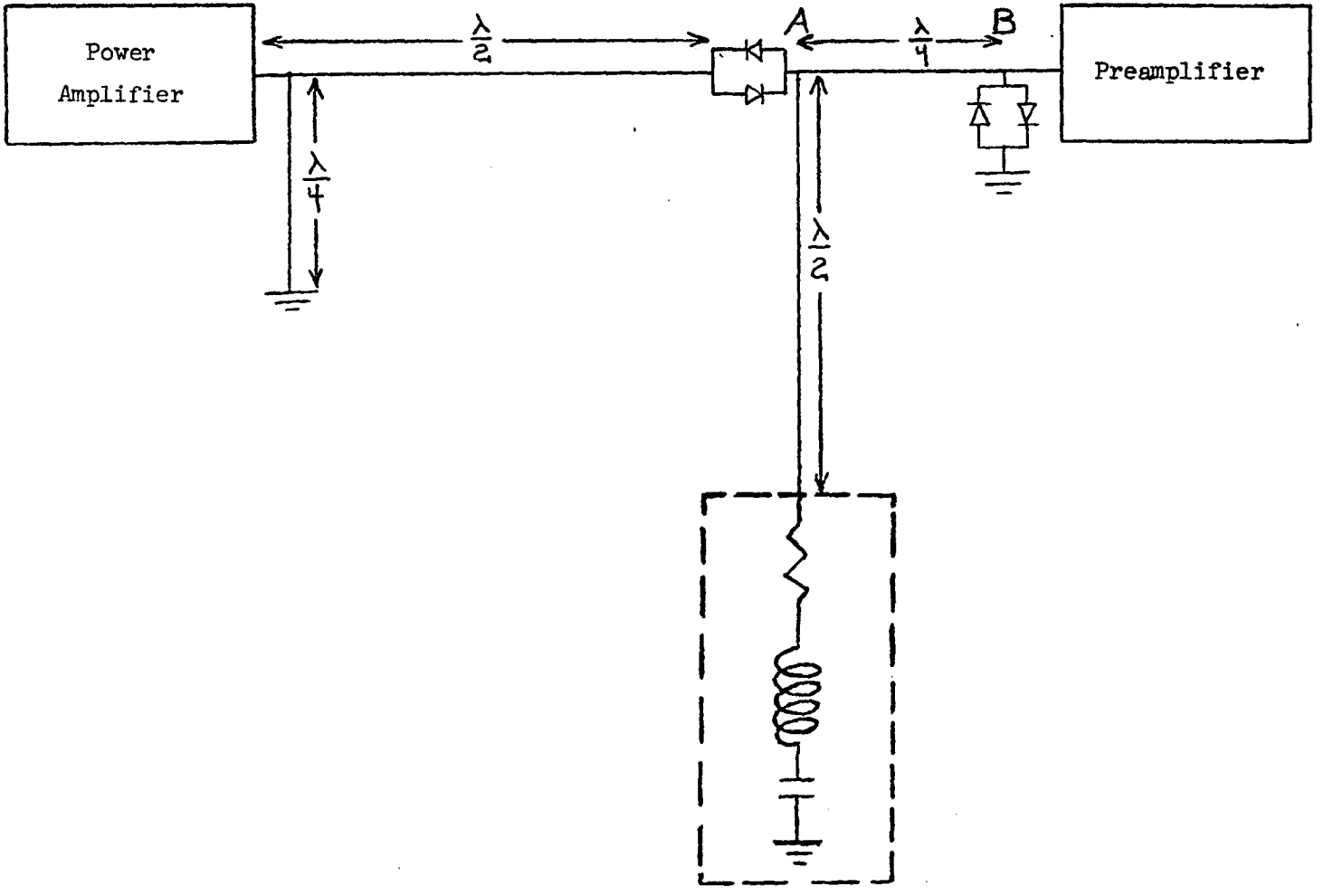
Power
Amplifier
λ/2
A
λ/4
B
Preamplifier
λ/4
λ/2
Probe

another half wavelength cable connects to the probe. There is another quarter wave cable between the diode shunt at A and a diode short located at the preamplifier input B. It is this quarter wave cable that enables the operation of the duplexer. When the power amplifier is on, both sets of diodes are conducting. The diode short at B is reflected as a large impedance at A. Thus the rf power is channeled to the probe. After the rf pulse damps the diodes no longer conduct. The diode shunt at A then presents a high impedance path to the power amplifier. Thus the NMR signal from the probe is directed to the preamplifier. The half wavelength cables minimize the effect of an impedance mismatch between transmitter and probe, and also ensure that the diode short at B does not appear across the coil.[21]

The single coil, series tuned probe used was cylindrical in shape, allowing a rotation within the magnetic pole gap. The probe is shown in Fig. 4. The initial design included a variable high-voltage capacitor using teflon as the dielectric. This was to enable the probe to be continuously tunable over a range of approximately 5 MHz. Unfortunately these capacitors could not withstand the rf power. Thus tuning was achieved only by removing turns from the coil or changing 6 kV fixed ceramic capacitors. At resonance, the probe impedance was 50 ohms, and the probe quality factor was approximately 5.

The probe coils were constructed with #24 gauge copper wire. They were roughly 3/4 inch in length with 27 turns. A teflon coil form was turned from a 1/2 inch diameter rod. It was sprayed with a silicon mold lubricant, and the coil was wound on it securely. Then a fast setting epoxy (Hysol 608) was applied to the coil. After 15 minutes the

Figure 4. Series-tuned Single Coil Probe. The copper rods are for mechanical support and electrical ground.

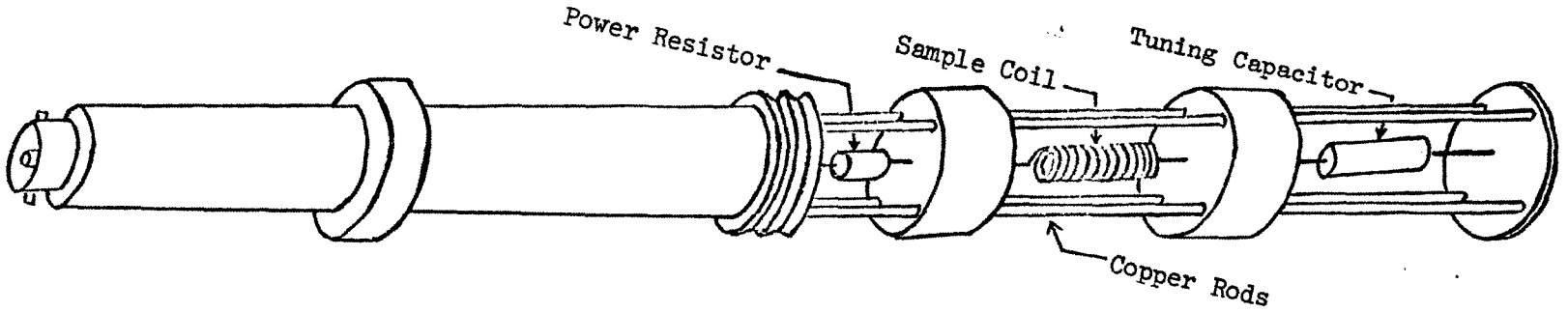
Power Resistor
Sample Coil
Tuning Capacitor
Copper Rods

epoxy was set, and the coil was removed from the form. This provided a uniform and virtually indestructable coil.

Recalling the sample size, one sees that the filling factor is not as good as it might be, but the FID signal is sufficient, and the rf homogeneity is excellent. The H_1 from a 2 kilowatt pulse is $\sim$75 gauss, making the pulse length for a 90° nutation of the Ga^{69} nuclei about 3.3 μsec. At 14.4 MHz the recovery of the spectrometer is $\sim$ 6 μ sec, making the total blocking time 10 μsec for a Ga^{69} FID. This is about 5% of the transverse relaxation time T_2.

Because the sample is piezoelectric, an unwanted transient signal is produced following the rf pulse. Without special precautions this distorted approximately the first 100 microseconds of the FID. It was suggested that such noise may be damped by placing the sample in contact with a fluid of appropriate viscosity. However it was easier, and just as effective, to surround the sample by a Faraday shield. The mylar strip was removed from a metallized mylar capacitor, enclosed in insulating tape, and wound closely around the sample coaxially with the rf coil. This reduced both the amplitude and the duration of the piezoelectric noise by an order of magnitude.

The signal to noise ratio (S/N) of the initial part of the FID following each 90° pulse was approximately 10, too small for accurate determination of the linewidths. So 5000 FID's were signal averaged to yield a S/N of over 700. The control instrumentation used to average the incoming data was designed and assembled in this laboratory. This system is unreported, so a more detailed description is found in Appendix B.

Briefly described, the FID undergoes analog-to-digital conversion in an 8 bit converter, a modified Computer Labs Model HS-802, at a rate of up to 5 MHz. Because this rate is too great for direct computer storage, the data for a single FID (1024 eight bit words) are stored in a buffer memory. Subsequent transfer to a Digital Equipment Corp. PDP 8/e minicomputer takes place during the NMR longitudinal relaxation time, T_1, at a rate set by the computer. The computer maintains storage of the most recent FID and the accumulated sum. Either of these may be displayed on an oscilloscope during T_1. When 5000 FID's have occurred, the computer transfers the accumulated data onto a nine track, industry compatible magnetic tape. The analysis of the data was performed with an IBM 360/50 computer.

The magnetic field was provided by a Varian V-3900 electromagnet and power supply equipped with Mark I Fieldial stabilization. This system was easy to adjust and stable, drifting less than 200 milligauss in eight hours after warmup. Magnetic field drift was monitored with the dual phase sensitive detector. At resonance, the FID component in quadrature with the transmitter rf is zero. Slightly off resonance, this component changes dramatically even though the in-phase component is not observed to change. It thus provides a sensitive measure of the magnetic field, and its use for this purpose insures that no FID distortion is caused by magnetic field drift.

IV. ANALYSIS

A. Determination of Isotropic and Angular Dependent Parts of Second Moments

Lowe and Norberg[22] have shown that the moments of the NMR line can be determined from the time derivatives of the FID at t = 0 by using the relation

$$\langle \Delta\omega^{2n} \rangle = \frac{(-1)^n}{g(0)} \left(\frac{d^{2n} g(t)}{dt^{2n}} \right)_{t=0} , \qquad (17)$$

where $\langle \Delta\omega^{2n} \rangle$ is the $2n^{th}$ moment and g(t) is the FID. However, the t = 0 point is precisely in the center of the rf pulse,[23] and the FID derivatives cannot be measured there directly. One method of obtaining second moments from the FID is to fit the visible part to an analytic function and to extrapolate back to t = 0 in order to evaluate the derivatives. The accuracy of this method, of course, depends upon the ability of the function to describe accurately the FID.

We used a least squares fitting routine[24] to fit the FID with two functions. The Abragam function

$$g(t) = \exp(-\alpha^2 t^2/2) \sin \beta t / \beta t \qquad (18)$$

was found to approximate the F^{19} free induction decay in CaF_2 very well.[25]

Our data appear qualitatively similar to the fluorine FID. However, when the Abragam function was fit to GaAs FID's, there were systematic deviations. Figure 5 shows the generally unsatisfactory character of the fits of this function. The Abragam function is successful in describing the FID shape of a spin 1/2 system broadened only by the like-spin dipolar interaction. It is a parametrization without rigorous theoretical foundation, but which works well in CaF_2. In the presence of other nuclear isotopes and other broadening mechanisms, there is little reason to expect that the Abragam function would continue to fit the FID.

However, if the quadrupole interaction is the chief reason that the Abragam function fails, then one can argue in favor of another functional form that does fit well to the GaAs FID. For half odd integral spins the first order effect of an efg is to leave the transition between the 1/2 to -1/2 energy levels unchanged and to split the other transitions into satellites. If the efg is random this leaves the central component of the line unaffected while the remainder of the line broadens. Thus the FID has a fast decaying component arising from the satellites and a slower decaying component arising from the central component. The GaAs FID may be better described by a sum of two Abragam functions. The function

$$g(t) = \left[I_1 \exp(-\alpha_1^2 t^2/2) + I_2 \exp(-\alpha_2^2 t^2/2)\right] \sin\beta t/\beta t \qquad (19)$$

agrees well with the observed FID. This is shown in Figs. 6 and 7. The angular frequency second moment of a FID described by Eq. (19) is

$$\tfrac{1}{3}\beta^2 + (I_1\alpha_1^2 + I_2\alpha_2^2)/(I_1 + I_2).$$

Figure 5. Ga^{69} FID and best functional fit using Abragam function.

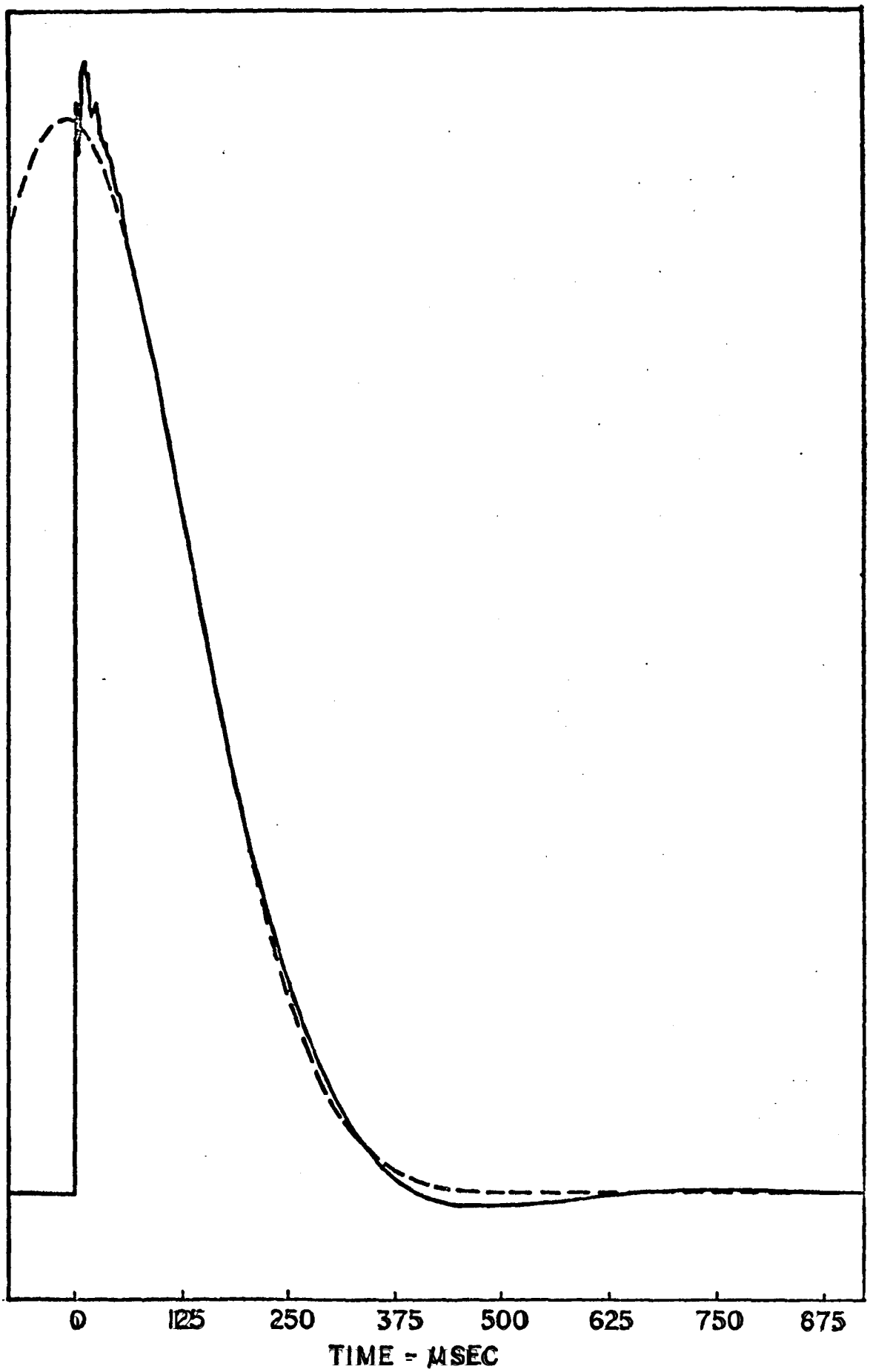
0
125
250
375
500
625
750
875
TIME - μSEC

Figure 6. As^{75} FID's and functional fit (dashed line) using Eq. (19) for samples a) M7U (undamaged), and b) M7D600 (quenched from 600°C). In both cases the Zeeman field is aligned with the [001] direction ($\theta = \pi/2$). The inset shows the indicated part of the curve with the vertical axis enlarged by a factor of 10. In this orientation the FID is not affected by damage.

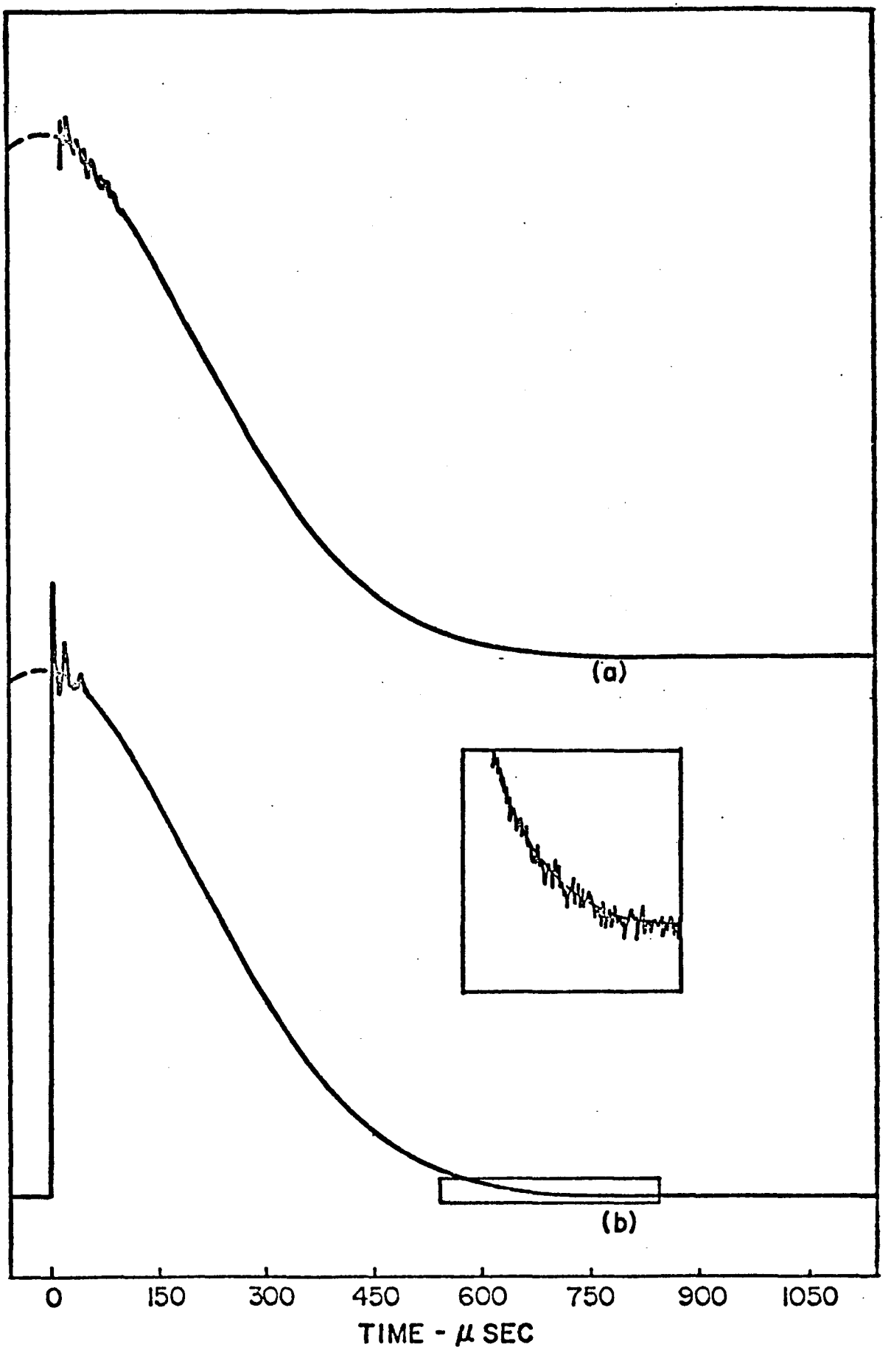
(a)
(b)
0
150
300
450
600
750
900
1050
TIME - μ SEC

Figure 7. As^{75} FID's and functional fit (dashed line) using Eq. (19) for samples a) M7U and b) M7D600. In both cases the Zeeman field is aligned with the [111] direction ($\theta = \cos^{-1}(3^{-\frac{1}{2}})$). The inset shows the indicated portion of the plot with the vertical axis enlarged by a factor of 10. The effect of the damage is evident.

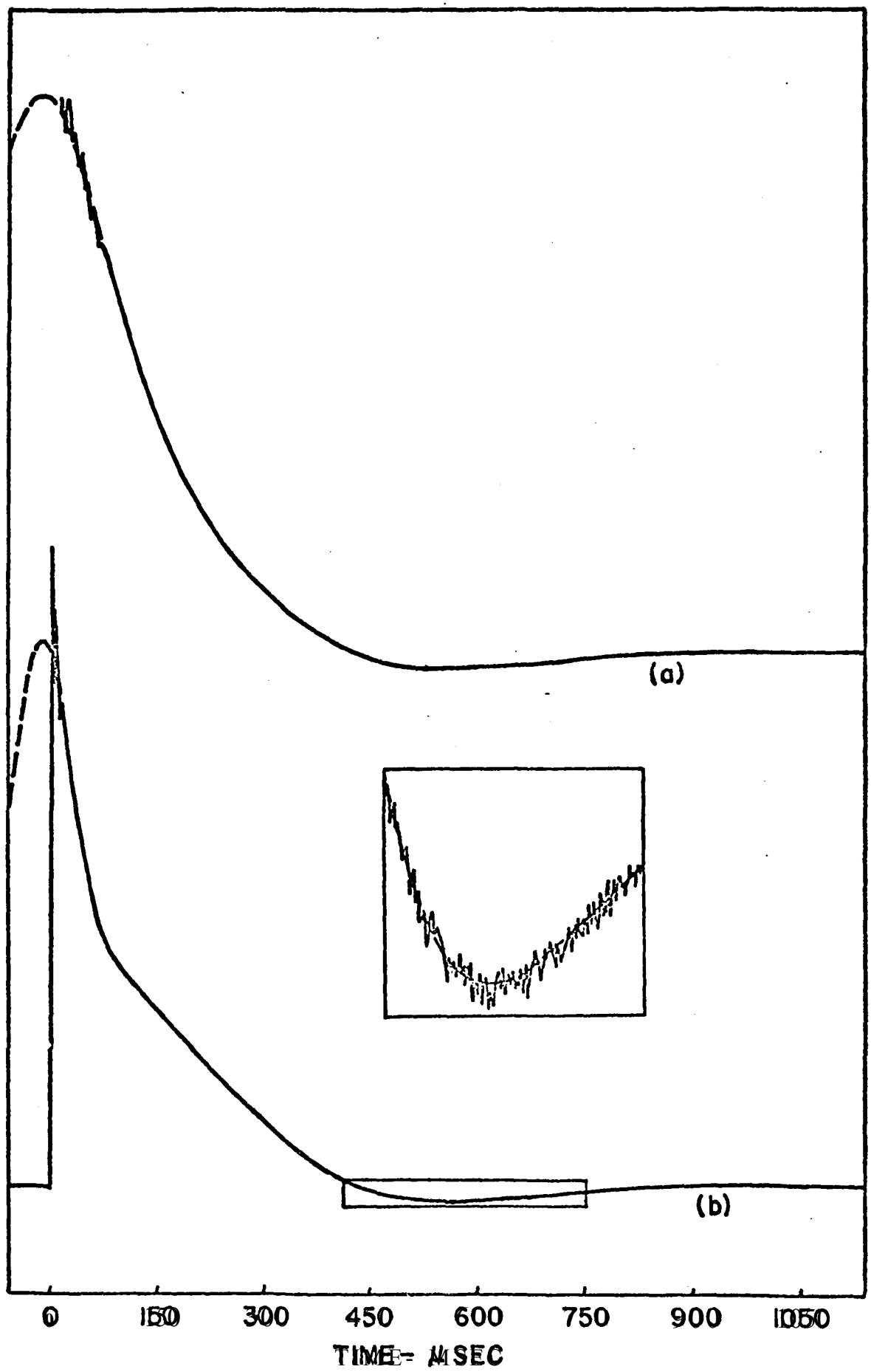
(a)
(b)
0
150
300
450
600
750
900
1050
TIME - μSEC

In the case of spin 3/2 nuclei, the satellite lines make up 60% and the central component 40% of the total resonant absorption. Thus one might expect to find $I_1/I_2 = 2/3$ and $\alpha_1 < \alpha_2$. This condition corresponds to 60% of the FID decaying faster than the other 40%. This is predicted by a lineshape calculation outlined in Appendix C. However, it is not experimentally the case. We find that the ratio I_1/I_2 departs from the value 2/3 with increasing quadrupole interaction. The quadrupole moments shown in Table I obey the inequality $Q_{75} > Q_{69} > Q_{71}$. In all samples, the As^{75} FID is described by Eq. (19) with $I_1/I_2 > 2/3$. This is also true of the Ga^{69} and, to a lesser extent, the Ga^{71} FID in those samples with large defect concentrations. As a result of the deviation of the fitting parameters from the behavior predicted by the calculation in Appendix C, we do not attempt to interpret the parameters physically. However, since Eq. (19) behaves as t^2 for small t and fits well to the observed FID, the second moments obtained are accurate. Only the second moments are used in the following analysis.

It was shown in Section II that a rotation of the magnetic field about the $[1\bar{1}0]$ direction results in the second moment varying as $C+Df(\theta)$. The contributions to the isotropic part C are from the dipolar and exchange mechanisms, while the contributions to D are from the dipolar, pseudodipolar and quadrupolar mechanisms. Parts C and D were determined by fitting the measured second moments at known θ to the function

$$\langle \Delta H^2 \rangle (\theta) = C + D f(\theta - \theta_0), \qquad (20)$$

TABLE I. RELEVANT NUCLEAR PROPERTIES[a]

Isotope	Natural Abundance (%)	I	Magnetic Moment (μ_N)	Electric Quadrupole Moment (barns)	R_{14}[b] (10^{10} cm^{-1})
Ga^{71}	39.8	3/2	2.5549	.12[c]	1.06[e]
Ga^{69}	60.2	3/2	2.0108	.19[c]	1.28[e]
As^{75}	100.0	3/2	1.4349	.29[d]	1.72[e]

[a] F. Bovey and A. Tiers, NMR Tables (Wiley-Interscience, Inc. New York 1967), 5th ed.

[b] The magnitude of coupling constant relating efg to applied electric field is adjusted for the given values of quadrupole moment.

[c] G. F. Koster, Phys. Rev. 86, 148 (1952).

[d] V. S. Korolkov, A. G. Makhanek, Opt. Spectry. USSR (English Transl.) 12, 87 (1962).

[e] D. Gill and N. Bloembergen, Phys. Rev. 129, 2398 (1963).

Generally, sixteen orientations covering a rotation of 120° were used to determine C and D. However, in samples with large defect concentrations only the orientations close to $\Theta = \pi/2$ were used, as few as six orientations. Figures 8, 9, and 10 show the second moments versus orientation for several samples.

The additional parameter, Θ_o, allows the second moment data to determine the absolute orientation of the crystal. This is a more accurate method than the initial alignment of the [001] axis with the magnetic field. The initial alignment ensures that a rotation study includes the orientations where the Zeeman field is aligned with the three major symmetry axes. Then the NMR data serve to determine the value of Θ_o. Thus any alignment error will have no consequence on the constants C and D.

Table II contains the coefficients C and D for each isotope in each sample. The same fitting routine that yields the constants C and D also determines their uncertainties.[24] These standard errors depend on the errors associated with the second moments at each orientation. Because there exists no theoretically justified shape for the FID, the error in the second moment is due to an incorrect choice of shape, not a statistical uncertainty. This makes the error in each second moment difficult to estimate. In order to make an estimate, several FID's were observed in a single orientation. Analyzing each individually showed that the second moment has a standard deviation of at most 10%. This value was inserted into the fitting routine determining C and D. The parameters C and D are

Figure 8. Ga^{71} second moments vs. Θ for samples listed in Table II. The solid lines are the best fits of Eq. (20). Only representative data points are shown.

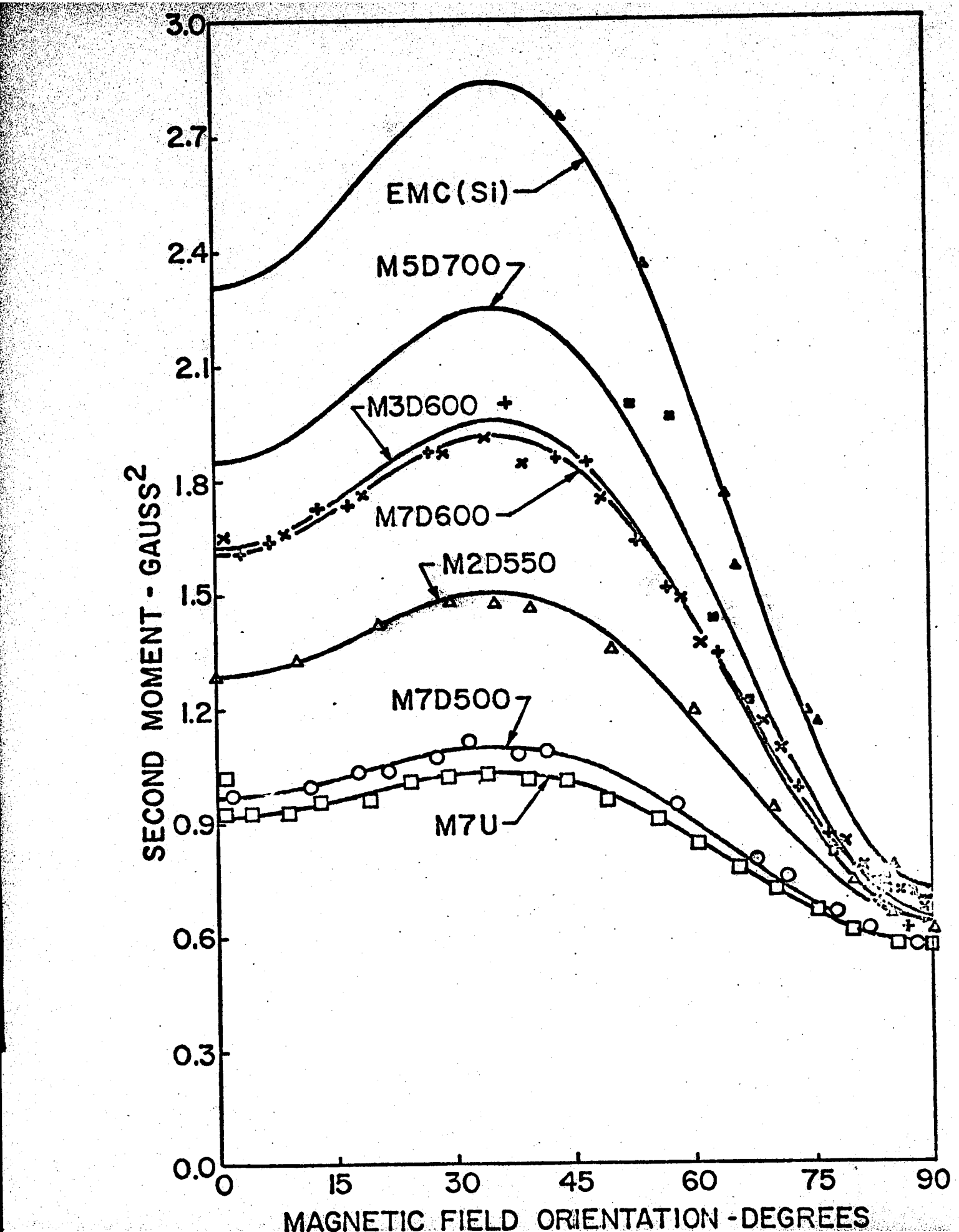
3.0
2.7
2.4
2.1
1.8
1.5
1.2
0.9
0.6
0.3
0.0
SECOND MOMENT - GAUSS^2
EMC(Si)
M5D700
M3D600
M7D600
M2D550
M7D500
M7U
0
15
30
45
60
75
90
MAGNETIC FIELD ORIENTATION - DEGREES

Figure 9. Ga^{69} second moments vs Θ . The solid lines are the best fits of Eq. (20). Only representative data points are shown.

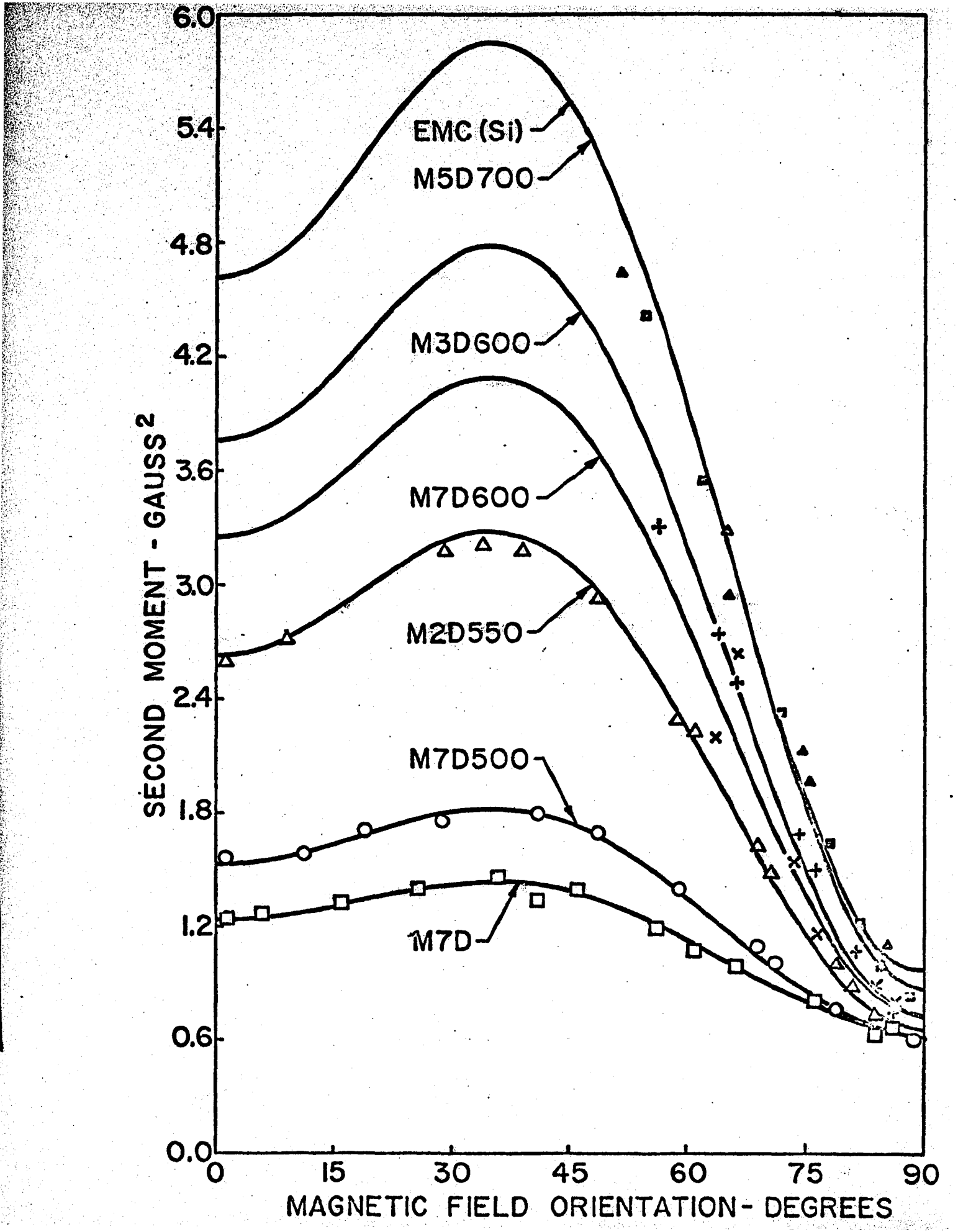
6.0
5.4
4.8
4.2
3.6
3.0
2.4
1.8
1.2
0.6
0.0
SECOND MOMENT - GAUSS²
EMC (Si)
M5D700
M3D600
M7D600
M2D550
M7D500
M7D
0
15
30
45
60
75
90
MAGNETIC FIELD ORIENTATION - DEGREES

Figure 10. As^{75} second moments vs. Θ . The solid lines are the best fits of Eq. (20). Only representative data points are shown.

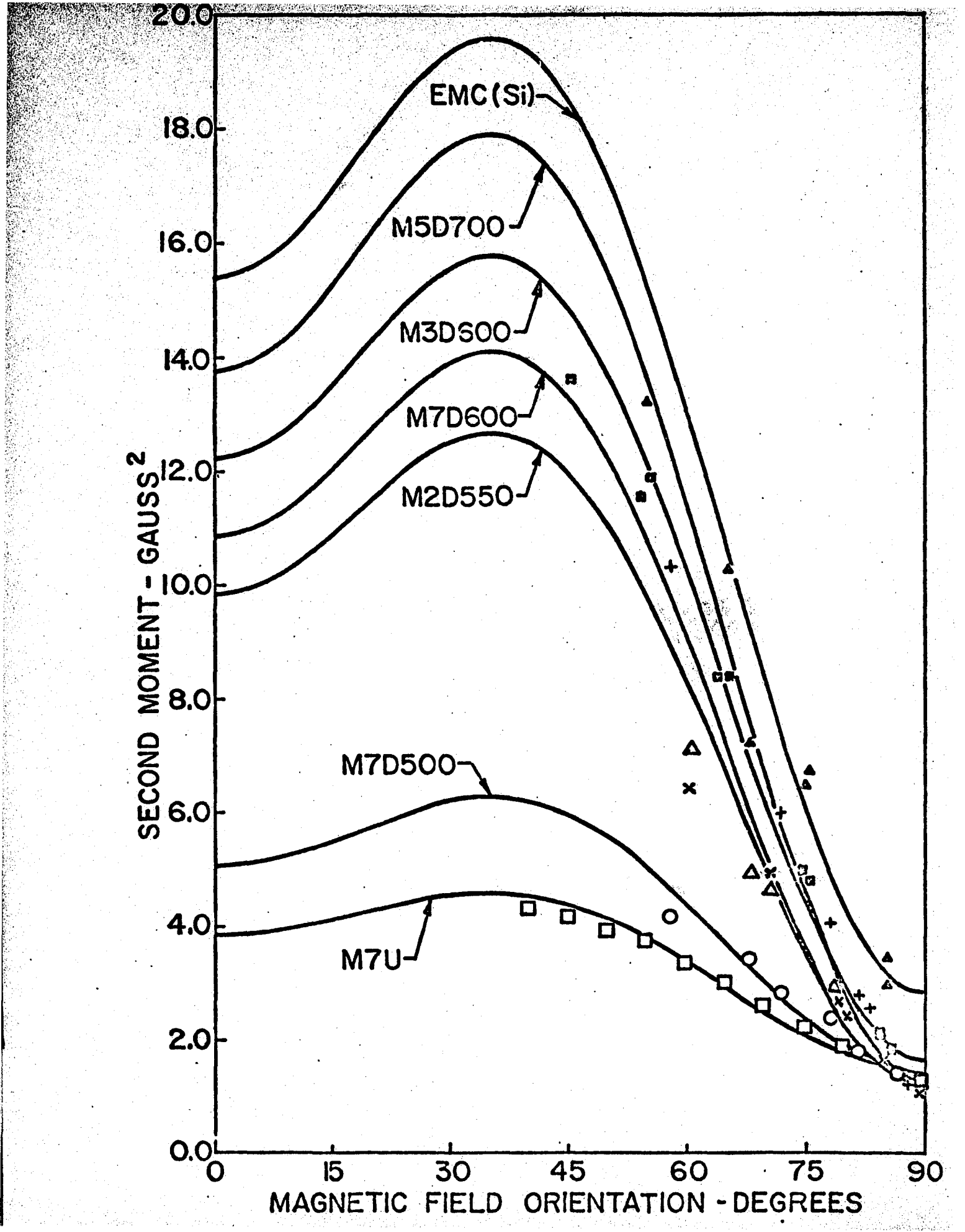
EMC(Si)
M5D700
M3D600
M7D600
M2D550
M7D500
M7U
SECOND MOMENT - GAUSS²
MAGNETIC FIELD ORIENTATION - DEGREES
0.0
2.0
4.0
6.0
8.0
10.0
12.0
14.0
16.0
18.0
20.0
0
15
30
45
60
75
90

TABLE II. MEASURED SECOND MOMENTS AS A FUNCTION OF MAGNETIC FIELD ORIENTATION. THE SECOND MOMENT IS EXPRESSED AS C + D $f(\Theta)$ IN UNITS OF GAUSS^2

Sample[a]	Ga^{71}		Ga^{69}		As^{75}	
	C	D	C	D	C	D
M7U	.58±.02	.68±.06	.64±.03	1.18±.08	1.44±.07	4.73±.36
M7D500	.58±.03	.77±.08	.63±.01	1.79±.02	1.40±.10	7.30±.85
M7D600	.63±.04	1.98±.13	.72±.04	6.08±.45	1.30±.14	24.9±1.61
M2U	.64±.03	.63±.07	.64±.03	1.22±.10	1.32±.07	5.58±.66
M2D550	.64±.03	1.30±.10	.66±.04	3.92±.19	1.23±.08	17.2±1.23
M3U	.65±.04	.69±.10	.72±.03	1.30±.11	1.37±.01	4.63±.04
M3D600	.69±.01	1.84±.03	.72±.04	5.05±.51	1.15±.08	19.4±1.60
M5D700	.65±.04	2.40±.23	.88±.07	7.46±.58	1.66±.14	21.2±1.14
EMC(Si)	.72±.05	3.18±.29	.95±.08	7.34±.73	2.83±.23	25.1±2.34

[a]Sample identification M2D500 means a Monsanto crystal quenched from 500°C. Undamaged samples are labeled with a U. EMC(Si) is a Si doped sample purchased from Electronic Materials Corp. with a carrier concentration of 4×10^{16} cm^{-3}.

statistically independent, and the function is linear in them. Thus, the standard deviation associated with C is, for example, $\sigma_C^2 = \sum_i \sigma_i^2 \cdot (\partial C/\partial y_i)^2$. This is the uncertainty found by the fitting routine, and is the corresponding diagonal element of the error matrix.

B. Identification of Contributions

Given the isotropic and angular dependent parts, the second moment contributions from the different broadening interactions may be identified. The pure van Vleck dipolar contributions are well known, and they are for each isotope:

$$\langle \Delta H^2 \rangle_D^{71} = .29 + 1.28 f(\theta) \quad \text{gauss}^2, \tag{21a}$$

$$\langle \Delta H^2 \rangle_D^{69} = .29 + 1.27 f(\theta) \quad \text{gauss}^2, \tag{21b}$$

$$\langle \Delta H^2 \rangle_D^{75} = .25 + 2.74 f(\theta) \quad \text{gauss}^2, \tag{21c}$$

where the subscript denotes the broadening mechanism, and the superscript the isotope. NAR data[7] on GaAs yield exchange coupling constants. Including only nearest and next nearest neighbor interactions, the unlike exchange contributions to the second moments are

$$\langle \Delta H^2 \rangle_E^{71} = .25 \text{ gauss}^2, \tag{22a}$$

$$\langle \Delta H^2 \rangle_E^{69} = .24 \text{ gauss}^2, \tag{22b}$$

$$\langle \Delta H^2 \rangle_E^{75} = .58 \text{ gauss}^2. \tag{22c}$$

Subtracting the contributions (21) and (22) from our data leaves only

the contributions from the quadrupolar and pseudodipolar interactions. The discussion in Section II predicts that these two contributions will have no isotropic part, and, as can be seen from Table II and Eqs. (21) and (22), the isotropic remainder is negligibly small for the two Ga isotopes. In nuclei of larger quadrupolar moments however, the isotropic remainder is larger than predicted on the basis of dipolar and exchange contributions.

In order to separate the contributions from the quadrupolar and pseudodipolar interactions one uses the fact that the pseudodipolar broadening in gauss^2 is the same for both Ga isotopes. This is because only the four nearest neighbors, all As nuclei, contribute significantly to the pseudodipolar broadening. Then the difference in the remaining angular parts of the Ga second moments must be due to quadrupolar broadening. Both Ga isotopes experience the same random efg, so the difference in their quadrupolar contributions must be due to the difference in their nuclear properties. Since $\langle \Delta H^2 \rangle_Q \propto Q_I^2/\gamma_I^2$, we may write that

$$\langle \Delta H^2 \rangle_Q^{69} = K \langle \Delta H^2 \rangle_Q^{71}, \tag{23}$$

where $K = (Q_{69}\gamma_{71}/Q_{71}\gamma_{69})^2$. If D_R^{71} and D_R^{69} are the remaining angular parts of the Ga^{71} and Ga^{69} second moments, respectively; then

$$\langle \Delta H^2 \rangle_Q^{71} = (K-1)^{-1}(D_R^{69} - D_R^{71}). \tag{24}$$

The relevant nuclear properties are shown in Table I. The values of R_{14} have been adjusted for more recent values of electric

quadrupole moment. Gill and Bloembergen give different numbers for the values of R_{14} for the two Ga isotopes. Physically we see no grounds for this difference, and thus a weighted average value of 1.2×10^{10} cm^{-1} is used for both. The Ga^{69} value is weighted more because the experiment on Ga^{69} was probably more accurate, due to the better S/N and the greater quadrupole shift. Another experimental measurement of R_{14} has been performed.[14] In that experiment R_{14} was measured dynamically by observing the nuclear transitions caused by an rf electric field. The evaluation of R_{14} is not as straightforward as the frequency measurement of Gill and Bloembergen. For this reason the static measurements of R_{14} are used here.

Once $\langle \Delta H^2 \rangle_Q^{71}$ and $\langle \Delta H^2 \rangle_Q^{69}$ have been established we may find the Ga pseudodipolar contribution

$$\langle \Delta H^2 \rangle_p^{71} = \langle \Delta H^2 \rangle_p^{69} = (K-1)^{-1} (K D_R^{71} - D_R^{69}) . \tag{25}$$

Comparing Eqs. (25) and (9), we obtain a quadratic expression for the pseudodipolar coupling constant $\tilde{B}_{NN}$ in terms of D_R^{71} and D_R^{69}. There are two solutions for $\tilde{B}_{NN}$, and this experiment cannot distinguish between them. In the case of GaAs both solutions are negative in sign.

The pseudodipolar interaction between nearest neighbors is symmetric, and is proportional to the magnetic dipole moments of the interacting nuclei.[5] Thus we may write

$$\langle \Delta H^2 \rangle_p^{75} = (.4\gamma_{71}^2 + .6\gamma_{69}^2)\gamma_{75}^{-2} \langle \Delta H^2 \rangle_p^{71} , \tag{26}$$

where .4 and .6 are the relative abundances of Ga^{71} and Ga^{69}, respectively. The quadrupolar second moment contribution is just the remaining angular part, D_R^{75}, less the pseudodipolar contribution $\langle \Delta H^2 \rangle_\rho^{75}$. With the quadrupolar contributions to the second moments determined, we may calculate the concentration of charged defects. For nuclear spin I = 3/2, Eq. (16) reduces to

$$\langle \Delta H^2 \rangle_Q = \frac{1}{10} \left(\frac{e e^* R_{14} Q_I}{\epsilon \gamma_I h} \right)^2 \left(\frac{\rho_I}{\rho} \right) f(\theta) \sum_j r_j^{-4} . \qquad (27)$$

The defect density ρ_I is found from Eq. (27) by equating the experimental $\langle \Delta H^2 \rangle_Q$ with this expression for the quadrupolar second moment. Table III contains the measured quadrupolar second moments, the pseudodipolar coupling constant, and the charged defect densities for each sample. The errors in Table III are calculated using the variances of the quantities C and D for all three isotopes and the standard theory of propagation of error.

Agreement of the defect densities as measured by Ga and As resonances is obtained only if we assume that the defects are preferentially located on the As sublattice. When this is true, the As nuclei are generally further from a defect than the Ga nuclei and will experience a smaller quadrupolar interaction. The value of the lattice sum in Eq. (27) depends upon which sublattice contains the defects. A single defect concentration accounts for the quadrupolar second moments for all isotopes only if this lattice sum is over the equivalent sublattice for As and the nonequivalent sublattice for Ga nuclei.

TABLE III. QUADRUPOLAR SECOND MOMENTS, DEFECT DENSITIES, AND PSEUDODIPOLAR COUPLING CONSTANTS. DEFECT DENSITIES ASSUME AN ARSENIC MONOVACANCY OF CHARGE e.

Sample	$\langle \Delta H^2 \rangle_Q$ (gauss^2) Ga^{71}	Ga^{69}	As^{75}	Defect Density (10^{15} cm^{-3}) As Measured By Ga	As	Pseudodipolar Coupling Constant $\tilde{B}_{NN}$
M7U	.17±.03	.67±.13	3.85±.41	.21±.04	.24±.03	-1.54, -.46±.05
M7D500	.34±.03	1.36±.11	6.62±.89	.42±.04	.42±.06	-1.47, -.53±.06
M7D600	1.33±.15	5.36±.62	23.7 ±1.70	1.65±.20	1.49±.11	-1.65, -.35±.12
M2U	.18±.04	.73±.16	4.75±.70	.22±.05	.30±.05	-1.52, -.48±.06
M2D550	.86±.07	3.48±.28	16.6 ±1.28	1.07±.09	1.04±.08	-1.48, -.52±.09
M3U	.20±.05	.81±.20	3.83±.34	.20±.06	.23±.02	-1.53, -.47±.08
M3D600	1.12±.17	4.51±.68	18.5 ±1.66	1.39±.21	1.16±.11	-1.57, -.43±.08
M5D700	1.67±.26	6.73±1.04	19.8 ±1.44	2.07±.32	1.25±.10	-1.70, -.30±.18

There are two facts which indicate that Frenkel pairs are rare in these samples. One is that the room temperature annealing is largely due to the recombination of Frenkel pairs,[12] and no annealing was observed. The other is that the lattice sum about a probable interstitial position is roughly equal for both sublattices. If this value were used in Eq. (27), the defect densities as measured by As and by Ga resonances would disagree.

An assumption in the calculation of the defect densities of Table III is that the effective charge of a defect is the electronic charge, or $e^* = e$. We assume a model in which the GaAs lattice is mostly covalently bonded, but retains some ionic character. The calculation of Harrison[26] yields a net charge of +0.87e on the Ga site and a net charge of -0.87e on the As site, where the electron has charge -e. If we remove a neutral As atom from the lattice and allow electronic charge shifts on only the four nearest neighbors, then each neighboring Ga ion acquires a net charge of 0.65e. Now there will be a certain ionization energy for these four neighboring Ga ions to collectively give up one electron to the conduction band and in the process acquire an additional .25e charge each. Then each Ga ion has a charge 0.9e, very nearly the 0.87e each had before the vacancy was produced. This small change in effective charge implies a small change in the bonding orbitals. On this basis we expect that the activation energy for ionization is small. The induced efg is sensitive to the change in the charge distribution. This difference is just 0.87e localized at the site of the As vacancy and +0.03e at each neighboring Ga site. This appears very much like a point charge defect to all nuclei, even the nearest Ga neighbors.

V. DISCUSSION

A. Pseudodipolar Interaction

The presence of the pseudodipolar interaction in III-V compounds has been recognized only recently.[8] One reason for this is that the nuclei in these compounds generally experience quadrupole interactions (P^{31} is the only exception). Since the magnetic field orientation dependence of the second moment contributions from each interaction has the form $C + Df(\Theta)$, the quadrupolar broadening can easily mask the effect of the pseudodipolar interaction. If the undamaged samples used in these experiments had a greater defect density, or if the pseudodipolar coupling constant had the same sign as the magnetic dipolar coupling constant, then the second moments of the Ga NMR signals would be larger than those calculated from the dipolar interaction alone. In that case there would be no clear evidence of the pseudodipolar interaction. It is now expected that the pseudodipolar interaction will be found in all III-V compounds.

There have been several theoretical treatments of electron coupled interactions, both from a band structure approach[4-6] and using localized bonding models.[13,27,28] Both approaches use second order perturbation theory. In order to calculate the coupling constants from band theory, greatly simplified band structures were used. Thus these calculations are very coarse. The localized bonding model calculations predict the negative sign of $\tilde{B}_{ij}$ observed in TlCl,[13] InP,[8] and now in GaAs.

However, these calculations do not agree quantitatively with our data or the InP data.

The method of Clough and Goldburg[13] begins by assuming a fixed degree of covalent character to the bonds. This covalent part of the bond is then represented by a variable admixture of s and p orbitals on each of the atoms contributing to the bond. They then find, using second order perturbation theory, an expression for the $\left| \tilde{B}_{ij}/\tilde{A}_{ij} \right|$ ratio as a function of the amount of s and p character in the bond. While the absolute magnitude of $\tilde{B}_{ij}$ and $\tilde{A}_{ij}$ depend upon the degree of covalency, λ, of the bond, the ratio $\left| \tilde{B}_{ij}/\tilde{A}_{ij} \right|$ is independent of λ. In their model they find that this ratio has a maximum value of 1/2 for purely p orbitals. Larger values have been measured in III-V compounds. Englesberg and Norberg[8] observed a $\left| \tilde{B}_{ij}/\tilde{A}_{ij} \right|$ ratio of 1.8 in a single crystal of InP and 1.5 in a powder sample. We measure a value of .73 or 2.2 in a single crystal of GaAs, depending upon which solution of Eq. (9) is physical.

Clough and Goldburg developed their expressions for TlCl crystals. One should not expect that the same model can accurately describe III-V compounds. The application of their model to GaAs has two major defects. It does not account for the d state admixtures in the wave functions that are known to be important. The second problem is that in polar semiconductors the wave function of valence electrons moves toward the anion[26] (As), while the wave function for the conduction band shifts toward the cation[29] (Ga). Since the exchange and pseudodipolar interactions are related to the overlap of the valence and conduction band wave functions, a model like Clough and Goldburg's, that assumes a fixed

covalent character to the bond for both the valence and conduction bands, will miss the consequences of the wave function shift between the cation and the anion. A modification of their calculation that accounts for the relative displacements of valence and conduction electron wave functions and the d state admixtures should be more accurate.

An alternative approach would be to repeat Harrison's calculation of the electronic wave functions, inserting the hyperfine interaction into the hamiltonian. This would allow one to calculate the hyperfine field at the nuclear site without second order perturbation theory. In this calculation the usual admixture of occupied and unoccupied electronic states is accomplished in the initial wave function, and no summation over all unoccupied states becomes necessary.

B. Quadrupolar Effects

An independent method of determining the charged vacancy concentration is desirable. Recently Logan and Hurle[30] have derived expressions that enable such a calculation. In their derivation they use standard methods of chemical thermodynamics[31] to obtain expressions for the equilibrium concentrations of As monovacancies, Ga monovacancies, Ga divacancies, and the charged versions of each. The concentration of each constituent is determined as a function of As_2 vapor pressure and temperature.

A brief description of their method follows. The reaction equations for the formation of each type of defect in the solid, the formation of electrons and holes, and the transfer of As atoms between the

gas and solid phases are written. At equilibrium one can then write a mass action equation for each reaction that relates the concentrations of its constituents. The additional condition of electroneutrality allows the solution of the concentrations of each defect in terms of the mass action equilibrium constants, temperature, and the vapor pressure of As_2.

Assuming that As monovacancies are the dominant species, the important reactions and corresponding mass action conditions are

$$V_{As}^{\circ} \rightleftharpoons V_{As}^{+} + e^{-} \; ; \; [V_{As}^{+}][e^{-}]/[V_{As}^{\circ}] = K_b , \tag{28a}$$

$$\tfrac{1}{2} As_2(gas) \rightleftharpoons As_{As}^{\circ} + V_{Ga}^{\circ} \; ; \; [V_{Ga}^{\circ}][As_{As}^{\circ}]/P_{As_2}^{1/2} = K_{As_2 V} , \tag{28b}$$

$$0 \rightleftharpoons V_{As}^{\circ} + V_{Ga}^{\circ} \; ; \; [V_{As}^{\circ}][V_{Ga}^{\circ}] = K_s , \tag{28c}$$

where the superscript indicates the charge, V_{As} an As vacancy, and As_{As} an As atom at an As site. Square brackets are used to indicate concentrations. The partial pressure of As_2 in the gas phase is designated P_{As_2}. It is noted that the partial pressures of the other vapor constituents are determined at equilibrium by the value of P_{As_2}, so their presence need not be taken into account explicitly. The mass action equilibrium constants (K_s, K_b, and $K_{As_2 V}$) have the usual exponential temperature dependence. The condition of electroneutrality we use is that the electron and As vacancy concentrations are identical,

$$[e^{-}] = [V_{As}^{+}] . \tag{29}$$

The solutions for the relevant concentrations may now be written

$$[V_{As}^{\circ}] = K_s / P_{As_2}^{1/2} K_{As_2 v}, \tag{30a}$$

$$[V_{As}^{+}] = [K_s K_b / P_{As_2}^{1/2} K_{As_2 v}]^{1/2}. \tag{30b}$$

Equations (30) demonstrate that an increase in the As_2 partial pressure decreases the vacancy concentration. Evaluation of the equilibrium constants at a given temperature and a given value of the partial pressure P_{As_2} completely determines the As vacancy concentration.

However, in this experiment, as well as those of Potts and Pearson, and of Driscoll and Willoughby,[32] the partial pressure of As_2 is not an independent variable. Initially the annealing vessel containing the GaAs crystal is evacuated, so the As_2 partial pressure results only from the production of As vacancies. The As_2 partial pressure and thus the As vacancy concentration become fixed functions of temperature.

Using the analysis of Logan and Hurle, the relation between the As_2 and As_4 partial pressures and the As vacancy concentration follows. Let the volume of the sample be v and the volume of the annealing vessel be rv. If n_2 and n_4 are the numbers of As_2 and As_4 molecules in the vapor, then

$$2n_2 + 4n_4 = v\, n_0 [V_{As}], \tag{31}$$

where n_0 is the molecular density in GaAs (2.2×10^{22} cm^{-3}), and $[V_{As}]$ is the mole fraction vacancy concentration. It is necessary to know the ratio

of As_4 to As_2 partial pressures. From vapor pressure data,[33] this ratio is given by

$$K_R \equiv P_{As_4}/P_{As_2} = n_4/n_2 = 4.67\, e^{-1980/T} . \qquad (32)$$

Combining Eqs. (31) and (32) yields

$$n_2 = \frac{\nu n_o}{2(1+2K_R)}[V_{As}] . \qquad (33)$$

Assuming an ideal gas law for As_2 the partial pressure is given by

$$P_{As_2} = \frac{n_o kT}{2(1+2K_R)}\,\frac{[V_{As}]}{r} = C'T\,[V_{As}], \qquad (34)$$

where $C' = n_o k/2(1+2K_R)r$.

The total As vacancy concentration $[V_{As}]$ is a sum of $[V^o_{As}]$ and $[V^+_{As}]$ given by Eqs. (30). Combining Eqs. (30) and (34) one obtains an equation for As_2 partial pressure

$$P^{3/2}_{As_2} - C'T\left[(K_s K_b/K_{As_2}\nu)^{1/2} P^{1/4}_{As_2} + (K_s/K_{As_2}\nu)\right] . \qquad (35)$$

This equation can be solved numerically at any given temperature. Once P_{As_2} is determined its value is inserted into Eq. (30b) to yield the charged As monovacancy concentration.

In the determination of P_{As_2} the assumption that the GaAs solid does not decompose is implicit. However if the As defect concentration

becomes sufficiently large, the GaAs crystal will reach its maximum possible deviation from perfect stoichiometry. Then any additional increase in the As vacancy density forces the crystal to decompose, and liquid Ga will form in the annealing vessel. The maximum $[V_{As}]$ is fixed by stoichiometry and is thus a function of temperature only. This limiting of $[V_{As}]$ fixes the As_2 partial pressure. The result is that Ga liquid will collect in sufficient quantity to maintain the equilibrium As_2 partial pressure. This is the equilibrium As_2 pressure on the liquidus curve, $P_{As_2}(eq)$, and it is the minimum As_2 partial pressure for a given temperature. If the As_2 partial pressure given by Eq. (35) is less than $P_{As_2}(eq)$, then there is decomposition, and $P_{As_2}(eq)$ must be used in Eq. (30b). This is the case in our experiment.

As long as the equilibrium in the annealing vessel is on the binary liquidus, the As vacancy concentration should be independent of the volume of the vessel. In order to test this prediction two samples were annealed at 600°C in vessels of different volumes. The defect densities have no annealing vessel volume dependence within experimental error.

The Arrhenius plot of the defect density is shown in Figure 11. In the upper left corner are the data of Potts and Pearson[12] along with the predicted vacancy concentration of Logan and Hurle[30] (solid line). Below are the data of Driscoll and Willoughby.[32] It is presumed that the difference in defect densities observed in these two experiments is due to the slow quench period (10 seconds) used by Driscoll and Willoughby. At these temperatures ionic mobilities are great enough to allow substantial

Figure 11. Log of the As vacancy concentration vs. the inverse quench temperature. Also shown are the data of Potts and Pearson[12] □ ; and Driscoll and Willoughby,[32] ■ . The solid line is the As vacancy concentration predicted under their experimental conditions by Logan and Hurle. The dashed line is the prediction of the ionized As vacancies under our experimental conditions using the same theory. ● and ○ represent our defect concentrations as measured by Ga and As resonances respectively.

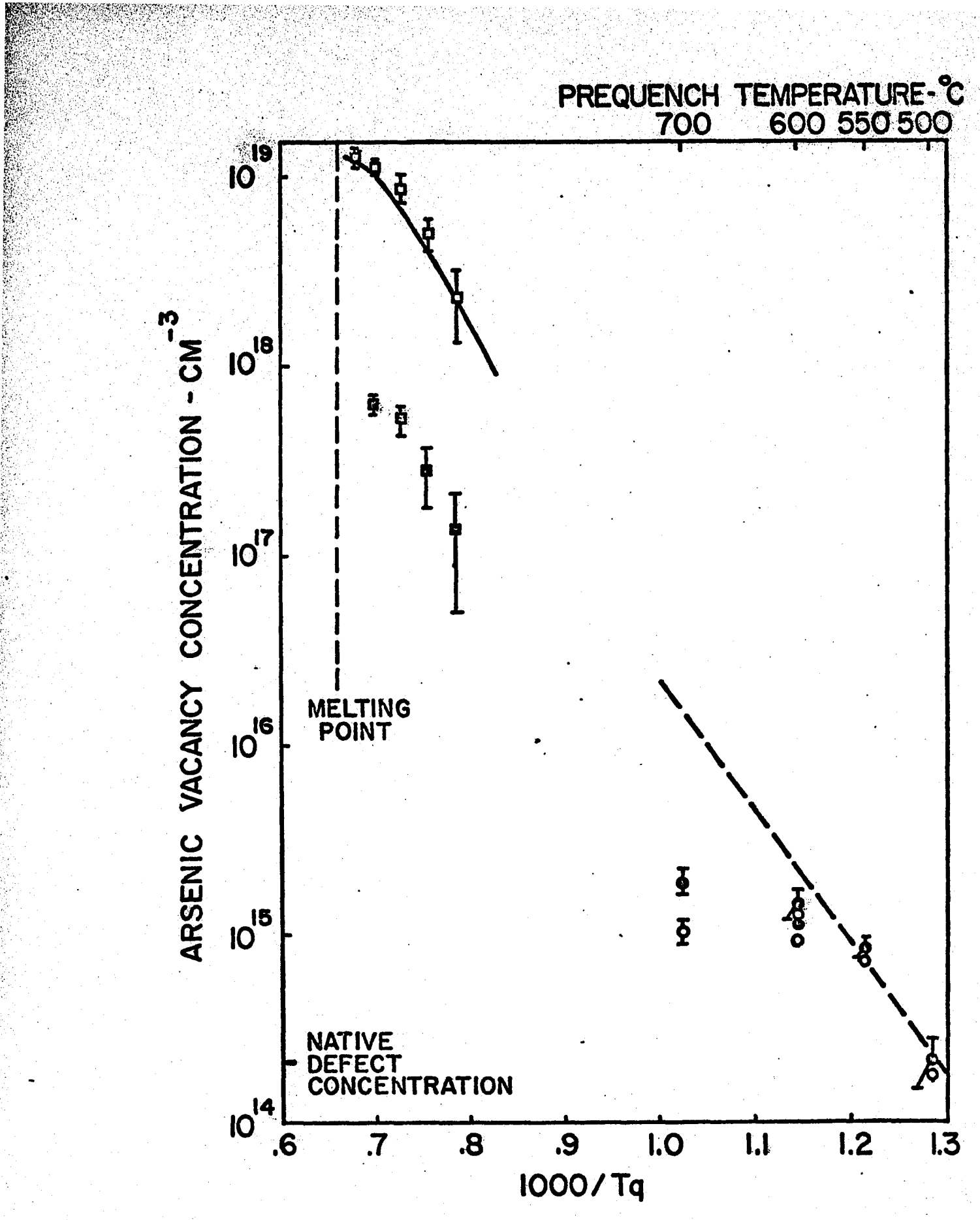
PREQUENCH TEMPERATURE-°C
700
600
550
500
ARSENIC VACANCY CONCENTRATION - CM⁻³
10¹⁹
10¹⁸
10¹⁷
10¹⁶
10¹⁵
10¹⁴
MELTING POINT
NATIVE DEFECT CONCENTRATION
.6
.7
.8
.9
1.0
1.1
1.2
1.3
1000/Tq

recombination during the quench period. This is not a problem at the lower temperatures that we used.

Our data are located in the lower right corner of Fig. 11. The dashed line is the charged As vacancy concentration calculated using the same theory that explains the data of Potts and Pearson, with no adjustable parameters. The standard deviations shown at each quench temperature are representative of all points at that temperature. These probable errors do not include errors in the quantities R_{14} and Q_I.

Prior to damage the samples had a native charged defect density, presumably due to ionized substitutional impurities. Since the carrier concentration in the sample is quite low we can assume that the electrons and holes produced by the impurities have annihilated. Thus the charged impurities cannot affect the concentrations of vacancies. However, our NMR measurement observes these charged defects. In order to compare to the predicted charged As vacancy concentrations, we must subtract the native defect concentration from the measurements following damage. This subtraction has been performed on our data shown in Fig. 11.

Our data tend to saturate at a defect concentration of 10^{15} cm^{-3}. The source of this saturation is not the same as the source of the saturation for Potts and Pearson. In our case the problem is an experimental limitation, while in the case of Potts and Pearson it is a real physical phenomenon. Their saturation occurs because at temperatures below 1400°C the annealing vessel had pressures greater than the equilibrium As_2 vapor pressure, but above 1400°C, P_{As_2} was the equilibrium vapor pressure $P_{As_2}(eq)$. This tends to saturate the As vacancy concentration.

Except at the highest quench temperature, our data seem adequately explained by the predicted concentrations of ionized As vacancies.

C. Experimental Limitation

It is possible that the low values of defect concentration measured in samples quenched at 600°C and 700°C are accurate. This effect could be caused by vacancy clustering or vacancy-acceptor pairing that is not evident in samples damaged at lower temperatures. However, it is more likely that these low values are due to the limitations in our current experimental technique and analysis. There are trends in the data that indicate that the present measurement of defect density errs if concentrations are larger than $\sim 10^{15}$ cm^{-3}. The increases in the second moment caused by thermal damage at 600°C and 700°C are proportionately smaller for nuclei with larger quadrupole moments. That is, the ratios of the increase in the Ga^{71} second moment to the increase in the Ga^{69} and As^{75} second moments are greater than expected. These ratios should be fixed by the nuclear properties. It is clear that the fast component of the FID decays so quickly in the presence of these large quadrupole interactions that our fitting analysis is not sensitive enough to it. This results in a deviation in the pseudodipolar coupling constant and a disagreement between the defect densities as measured by Ga and As resonances.

Additional evidence that this experiment cannot measure relatively large defect concentrations is seen in the data for the Si doped sample. The Ga^{69} second moments are much smaller than one expects from the large second moments of Ga^{71}. To an even greater extent, the same is true of

As^{75}. Assuming that the pseudodipolar interaction is the same in all GaAs crystals, and assuming that the ionized Si donors are located on Ga sites, then the Ga^{71} data indicate a charged defect density of 6.4×10^{15} cm^{-3}, where the Debye-Hückel screening has been taken into account. Hall effect measurements yield a carrier concentration of 4×10^{16} cm^{-3}, so there are at least that many ionized impurities. With the current experimental limitations, this technique is too sensitive to accurately measure charged defect concentrations greater than 10^{15} cm^{-3}.

It is concluded that the present experiment does not dependably measure frequency second moments larger than 5×10^6 Hz^2. This corresponds to a FID half width of approximately 70 μsec. Using the Ga^{71}, Ga^{69}, and As^{75} resonances this corresponds to charged defect densities of 2.5×10^{15} cm^{-3}, 9×10^{14} cm^{-3}, and 2×10^{14} cm^{-3}, respectively. In order to make equivalent cw measurements, a large S/N is required at least as far as 5 kHz from the center frequency. This is difficult to obtain when the resonance linewidth is $\sim$ 2 kHz. With improved damping of the piezoelectric noise and with spin locking techniques we expect these upper limits to be extended to charged defect densities near 10^{17} cm^{-3}. At these concentrations we expect that second order quadrupolar effects will be important, and that the lineshape will have changed substantially.

The lower limit of measurable charged defect concentration would occur where the quadrupole contribution to the As second moment is just measureable, say 0.1 $gauss^2$. This corresponds to a defect density of 6×10^{12} cm^{-3} on the As sublattice or 3×10^{12} cm^{-3} on the Ga sublattice, representing a defect to atom ratio of the order of 10^{-10}. When

this method is applicable, it rivals the sensitivity of neutron activation and Hall effect measurements. Unlike neutron activation measurements, the NMR method can observe electronically active vacancies. Unlike Hall effect measurements, the NMR method detects the total number of charged defects, not the net charge carrier concentration.

VI. SUMMARY

There remain questions about the structure and formation of defects in large concentrations, and these questions suggest further investigations. One important improvement of this experiment is to extend the range of defect concentration measurement to $\sim 10^{17} cm^{-3}$. The problem in the current work is that the FID decays significantly before it can be observed. This problem could be largely resolved if a zero time resolution technique[35,36] were employed. The entire FID would then be visible. Assuming that the rf magnetic field is large enough to nutate all nuclei coherently, the entire satellite contribution could be observed even in the presence of large defect concentrations. Then the range of measurement could be extended to 10^{17} cm^{-3} or possibly 10^{18} cm^{-3}.

In this experiment the defect concentrations were small, and the data are adequately explained by As monovacancies. However, in the presence of large defect concentrations there is a greater probability of forming defect clusters. The structure of defect clusters as well as the near neighbor electronic shielding can be probed in further investigations using the double resonance technique.[37] This technique is capable of detecting rare spin species (10^{15} cm^{-3}) by their effect on the resonance of an easily observable spin system. One can apply this method to detect the resonance frequency shift of the nuclei near to a defect, and in this way probe the structure and effective charge of the defect.

While questions remain about large defect concentrations in GaAs, this experiment has made several contributions toward the use of NMR as an accurate measurement technique. A straightforward point defect model was developed. Using this model, it was shown that the quadrupolar second moment contribution is linearly proportional to the charged defect density, and the proportionality constant was derived. In addition, the effect of the quadrupolar interaction on the FID lineshape was calculated.

Due to the existence of the pseudodipolar interaction, the second moment analysis had to separately identify the quadrupolar and pseudodipolar contributions. A technique using data from both Ga isotopes was successfully employed. That this analysis is correct is adequately demonstrated by two facts. One is that the pseudodipolar interaction, within experimental error, remains independent of the total second moment, i.e., thermal damage. The second is that the charged defect densities as measured by Ga and by As resonances agree for samples with small concentrations, where no FID fitting difficulties were encountered.

It has also been shown that the NMR second moment is extremely sensitive to defect concentrations in GaAs, and that measurements in compensated crystals are useful. The second moment is so sensitive that this first order line shape and second moment analysis are insufficient to treat samples of defect concentration greater than $\sim 10^{15}$ cm^{-3}. Furthermore, in a crystal of carrier concentration of 2.4×10^{11} cm^{-3}, this NMR technique measured a charged defect concentration of 2×10^{14} cm^{-3}. Since

the sum of the donor and acceptor concentrations are detected, it is clear that this NMR technique is of greater value in the measurement of defects in compensated crystals than are Hall effect measurements.

Finally, this research has demonstrated that As monovacancies are indeed generated in thermal quenching experiments and that they become ionized with an effective charge of $e^* = e$.

VII. ACKNOWLEDGEMENTS

I wish to express my gratitude to the following persons:

M. Schmidt and L. H. Botten for the design and construction of equipment;

M. K. Cueman, J. W. Kaufer, and P. A. Millington for assistance in taking the data;

S. J. Stout for the immaculate typing of this dissertation;

F. R. Crownfield, I. J. Lowe, and K. G. Petzinger for their time and care in the reading of this dissertation and for their helpful comments;

A. Sher for continued interest in this research and valuable discussions;

H. E. Schone for continued interest in this research and helpful lectures on the hyperfine interactions;

J. F. Soest for directing this research, and for serving as advisor, psychoanalyst, and ski instructor;

Peggy, my wife, for being the most patient spouse any person could possibly have during graduate school;

REFERENCES

1. J. H. van Vleck, Phys. Rev. 74, 1168 (1948).
2. R. G. Shulman, B. J. Wyluda, and H. J. Hrostowski, Phys. Rev. 109, 808 (1958).
3. R. G. Shulman, J. M. Mays, and D. W. McCall, Phys. Rev. 100, 692 (1955).
4. M. A. Ruderman and C. Kittel, Phys. Rev. 96, 99 (1954).
5. N. Bloembergen and T. J. Rowland, Phys. Rev. 97, 1679 (1955).
6. P. W. Anderson, Phys. Rev. 99, 623 (1955).
7. R. K. Sundfors, Phys. Rev. 185, 458 (1969).
8. M. Engelsberg and R. E. Norberg, Phys. Rev. B 5, 3395 (1972).
9. E. H. Rhoderick, J. Phys. Chem. Solids 8, 498 (1958).
10. M. Cohen, Phil. Mag. 3, 565 (1958).
11. D. Gill and N. Bloembergen, Phys. Rev. 129, 2398 (1963).
12. H. R. Potts and G. L. Pearson, J. Appl. Phys. 37, 2098 (1966).
13. S. Clough and W. I. Goldburg, J. Chem. Phys. 45, 4080 (1966).
14. E. Brun, R. J. Mahler, H. Mahon, and W. L. Pierce, Phys. Rev. 129, 1965 (1963).
15. R. L. Mieher, in Semiconductors and Semimetals, edited by R. K. Williardson and A. G. Beer (Academic Press, New York, 1966), vol. 2 chpt. 7.
16. R. Kubo and T. Nagamiya, Solid State Physics, (McGraw-Hill, New York, 1969), p. 690.

17. G. L. Pearson, H. R. Potts, V. G. Macres, Proceedings of the 7th International Conference on the Physics of Semiconductors, Damage of Semiconductors (Dunod et Cie., Paris, 1965), p. 197.

18. D. L. Kendall, in Semiconductors and Semimetals, edited by R. K. Williardson and A. G. Beer (Academic Press, New York, 1968), vol. 4, chpt. 3.

19. J. D. Ellett, M. G. Gibby, U. Haeberlen, L. M. Huber, M. Mehring, A. Pines, and J. S. Waugh, Advances in Magnetic Resonance 5, 117 (1971).

20. I. J. Lowe and C. E. Tarr, J. Sci. Instrum. (Series 2) 1, 320 (1968).

21. B. M. Moores and R. L. Armstrong, Rev. Sci. Instrum. 42, 1329 (1971).

22. I. J. Lowe and R. E. Norberg, Phys. Rev. 107, 46 (1957).

23. D. Barnaal and I. J. Lowe, Phys. Rev. Letters 11, 258 (1963).

24. P. R. Bevington, Data Reduction and Error Analysis for the Physical Sciences (McGraw-Hill Book Co., New York, 1969), chpt. 11.

25. A. Abragam, The Principles of Nuclear Magnetism (Oxford University Press, London, 1969), chpt. IV.

26. W. A. Harrison, Phys. Rev. B 8, 4487 (1973).

27. K. Yosida and T. Moriya, J. Phys. Soc. Japan 11, 33 (1956).

28. N. Bloembergen and P. P. Sorokin, Phys. Rev. 110, 865 (1958).

29. W. A. Harrison, private communication.

30. R. M. Logan and D. T. J. Hurle, J. Phys. Chem. Solids 32, 1739 (1971).

31. A. F. Kröger, Chemistry of Imperfect Crystals (North Holland, 1964), chpt. 13.

32. C. M. Driscoll and A. F. W. Willoughby, Proceedings of the International Conference on Radiation Damage and Defects in Semiconductors, Reading, Berks., England (London, England: Inst. Phys. 1973).

33. N. N. Sirota, in Semiconductors and Semimetals, edited by R. K.Willardson and A. G. Beer (Academic Press, New York, 1968), vol. 4, chpt. 2.

34. J. R. Arthur, J. Phys. Chem. Solids 28, 2257 (1967).

35. J. Jeener and P. Broekaert, Phys. Rev. 157, 232 (1967).

36. I. J. Lowe, K. W. Vollmers, and M. Punkkinen, Proceedings of the First Specialized "Colloque Ampere" (Krakow, Poland, August, 1973) (to be published).

37. A. Hartland, Proc. Roy. Soc. A 304, 361 (1968).

38. H. Cramer, Mathematical Methods of Statistics, (Princeton Univ. Press, Princeton, N. J., 1946), chpt. 17.

APPENDIX A

Pulse Programmer Description

The operation of the pulse programmer shown in Fig. 12 is based on a 256 bit random access memory divided into sixteen 8 bit words. Each step of a pulse sequence requires a single word of memory. In the eight bit word, four bits of a word specify the next memory address to be accessed, and four bits specify the function to be executed (a particular pulse or time delay). These four bit half words allow access of any memory address and execution of 16 individual functions. In operation, the memory words are retrieved in an order specified by the preceding word, executing the desired functions in that order. For example, a sequence step with memory contents 1A (hexadecimal notation) will execute function 1, and memory address A will be accessed on the next step.

During a read cycle, the function half word (four bits) is held stable in the function register that drives the inputs of a 1-of-16 decoder. The output of this decoder enables the timing device corresponding to the appropriate function. The next address half word is gated into the next address register, and later into the current address register in preparation for the next read cycle. All registers are composed of type JK flip-flops. The inputs are strobed with timing pulses.

The timing pulse generator controls the memory data read and write cycles. Four timing pulses are required whose durations and separations are details of the memory. The pulses are generated by monostable multivibrators (one shots).

Figure 12. Block Diagram of the Pulse Programmer.

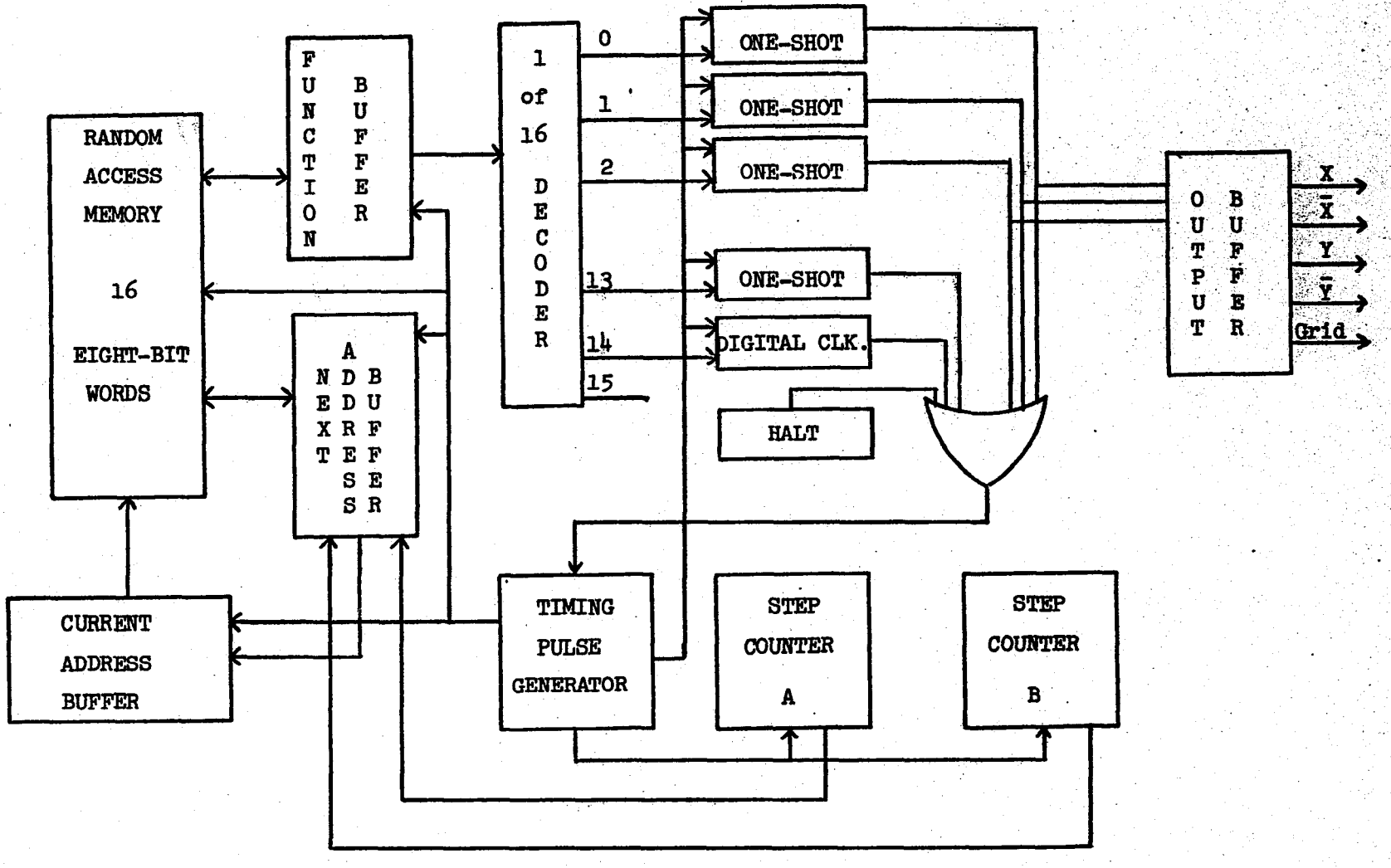
RANDOM ACCESS MEMORY
16
EIGHT-BIT WORDS
FUNCTION BUFFER
NEXT ADDRESS BUFFER
CURRENT ADDRESS BUFFER
1 of 16 DECODER
0
1
2
13
14
15
ONE-SHOT
ONE-SHOT
ONE-SHOT
ONE-SHOT
DIGITAL CLK.
HALT
TIMING PULSE GENERATOR
STEP COUNTER A
STEP COUNTER B
OUTPUT BUFFER
X
$\bar{X}$
Y
$\bar{Y}$
Grid

The memory read cycle is initiated when the timing device of an executing function terminates. The series of timing pulses then retrieves the memory data from the current address and executes the function specified in the function register. In addition the timing pulse generator increments the internal step counters once every read cycle. At the end of the four timing pulses, the timing generator stalls. It is reinitiated at the end of the currently executing function.

Any of the function timing devices must be able to trigger the timing generator, so the output of each drives an input of a 16-input OR gate. A negative-going edge of the output of this gate triggers the timing generator. One input of this OR gate is connected to the manual halt control. When held high, this input can inhibit negative going edges at the output. Then the timing generator cannot be retriggered, and the sequence halts. Programs may be executed one step at a time by manually triggering the timing generator while inhibiting negative-going edges at the output of the OR gate.

The memory write cycle is similar to the read,with the addition of a timing pulse that enables the alteration of memory data. Of course, internal initiation of the timing pulse generator is inhibited. Because the memory data registers also serve as contact debouncers for the data input lines, these registers must be cleared following each write cycle.

When in use, the two internal step counters override the memory inputs to the next address register. The counters overflow after counting a presettable number of steps. At overflow, counter B clears the next address register, making the contents of address 0 the next memory data

retrieved. This address must be programmed when counter B is in use. In a similar way, at overflow, counter A sets the next address register, and address 15 is thus the memory data retrieved. An important difference between counters A and B is that while B counts only sequence steps, A may also count the number of times that counter B overflows. In the event that both counters overflow simultaneously, counter A dominates.

All function timing devices are either one-shots or digital counters run by a 10 MHz clock. A function enabled by the decoder is initiated by the timing generator, and, upon completion, the function then initiates the timing generator. One-shot durations are controlled by potentiometers, and digital counters overflow at presettable times.

Time delays are distinct from pulses only by their function codes, and by the fact that no pulse outputs are derived from the time delays. Pulses have codes 0 - 7, and time delays, 8 - 15. Pulses 0 - 4 and delays 8 - 12 are controlled by one-shots. Delay 14 is a counter, and delay 15 is a programmed halt, so it has no timing device. Pulses 6 and 7 are controlled either by one-shots or the same counter used by 14. These are designed for digitally controlled spin-locking pulses. Functions 5 and 13 reset counters A and B, respectively. In addition function 13 is triggered on an edge of the clock signal that controls data acquisition to be described in Appendix B. This prevents time jitter between the experiment control and the data digitization.

The output signals of the pulse programmer are derived in the output buffer. Each time a pulse one-shot is initiated, a corresponding

flip-flop is set by a timing pulse, TP1. It remains set until the program executes another function, but it is reset only at TP1 time. This design eliminates the inevitable propagation time between the end of one function and the beginning of the next. For example, two sequential pulses may be desired with no time separation. The flip-flop outputs are buffered by power NAND gates that provide the current for the rf switches. Any gate may drive any one of the 4 rf switches.

The other output signals derived are to turn on the grids of the power amplifier and to protect the receiver rf amplifier from the power pulse, and they are buffered in the same manner.

APPENDIX B

Data Acquisition

The basic components of the data acquisition instrumentation are shown in Fig. 13. Each FID is digitally sampled up to 1024 times at a constant rate, so the FID may be reconstructed using the data in the 1024 equal time intervals. The digitizing rate is derived from a free-running 10 MHz crystal oscillator by a frequency divider. If this divider were also free-running with respect to the pulse sequence, then there would be an uncertainty in the time elapsed from the beginning of the rf pulse to each interval. The uncertainty would be half the period of the digitizing rate, and the actual error would vary for each FID.

In order to avoid this time jitter, the NMR pulse sequence is synchronized with the 10 MHz clock. The first step in a pulse sequence is time delay 13 (see Appendix A). The corresponding one-shot in the pulse programmer is enabled by the coincidence of the function decoder signal and the normal timing pulse that triggers the other function timing devices. Then on the next positive-going edge of the 10 MHz clock, delay 13 is triggered. Thus the pulse sequence begins coherently with the 10 MHz clock. In addition the leading edge of delay 13, after an adjustable delay, enables the frequency divider. Thus the data acquisition is coherent with the pulse sequence.

The delayed front edge of the 13 function, by enabling the divider, initiates the data acquisition for the current FID. At the same

Figure 13. Block Diagram of the Data Acquisition System.

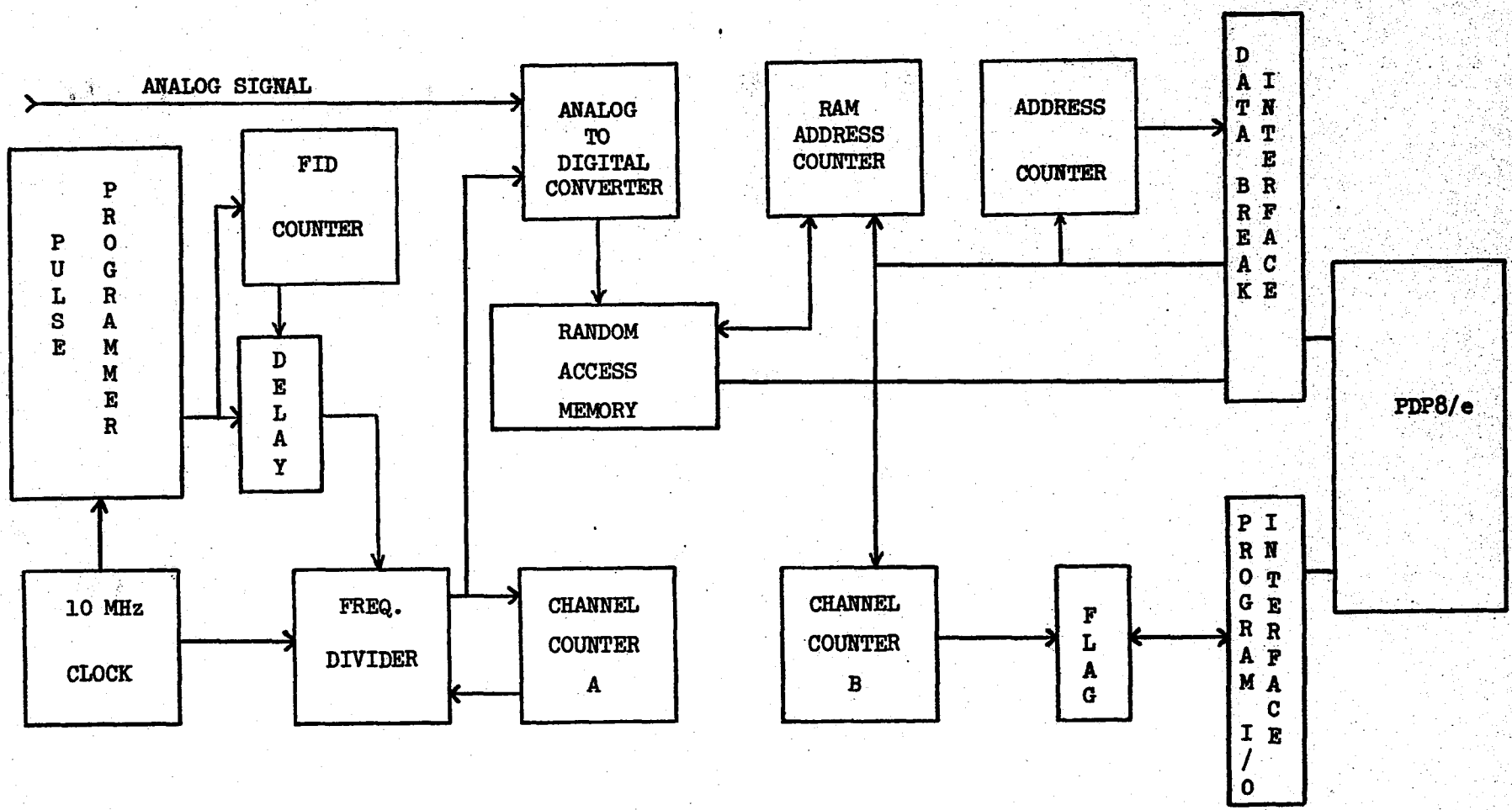
ANALOG SIGNAL
PULSE PROGRAMMER
FID COUNTER
DELAY
ANALOG TO DIGITAL CONVERTER
RAM ADDRESS COUNTER
ADDRESS COUNTER
DATA BREAK INTERFACE
RANDOM ACCESS MEMORY
PDP8/e
10 MHz CLOCK
FREQ. DIVIDER
CHANNEL COUNTER A
CHANNEL COUNTER B
FLAG
PROGRAM I/O INTERFACE

time a FID counter is decremented. This counter is preset to the number of FID's desired in a particular signal averaging run. When the counter reaches zero, the time delay is disabled, and all future signals from the programmer are ignored.

When enabled, the frequency divider produces pulses at the desired digitizing rate. These go directly to the analog-to-digital converter (ADC) and decrement Channel Counter A. On each pulse, the ADC begins digitizing a channel of the FID. When the ADC is finished (about 150 nanoseconds later) it issues a pulse storing the data in the Random Access Memory (RAM), and incrementing the RAM Address Counter. The Channel Counter is preset to the number of channels of FID data desired. The maximum is 1024. When the Channel Counter reaches zero, it disables the divider, halting the sampling of the FID. All counters are then reset, and the conversion stalls waiting for the next signal from the programmer.

Now the current FID in temporary storage is transferred to the minicomputer. The transfer is initiated by the signal from the Channel Counter A that also disables the divider. On this signal, the data break interface suspends the normal computer program and allows direct transfer of the data into the computer core memory. This is done synchronously with the computer timing.

A computer timing pulse transfers the data from the RAM into the computer memory address specified by the Address Counter, and increments both the RAM Address Counter and the computer Address Counter. At the same time Channel Counter B (preset to the number of channels of data) is

decremented. This process is continued, one data word transfered in each computer cycle, until Channel Counter B reaches zero. On a signal from Channel Counter B the computer resumes its program, all counters are reset, and the data transfer stalls waiting for the completion of the digitization of the next FID.

Now it is up to the computer program to add the new data, channel by channel, to the sum of the previous FID's. However, the data break transfer, while extremely fast (1.4 μsec/word), has the disadvantage that the program has no simple way of testing to see if a data break has occurred.

Our solution to this problem is to use the programmed data transfer interface. This allows the data acquisition program to test the status of a flag to determine if a data break has occurred. The flag is set by Channel Counter B signaling the end of a data break. When the program finds the flag set, it adds the current FID to the cumulative sum, resets the flag, and returns to a routine displaying the data on an oscilloscope.

APPENDIX C

The objective of this appendix is to compute the NMR line shape due to the quadrupolar interaction using a continuum crystal model. From Eqs. (3g), (12) and (13) the satellite frequency shift of a spin 3/2 nucleus located a distance r from a charged impurity is

$$\Delta\nu = -\vec{\alpha}\cdot\vec{r}/r^3, \tag{C1}$$

where

$$\vec{\alpha} = \frac{e\dot{e}^{*}QR_{14}}{\epsilon h}\left(\eta_y n_z \hat{x} + \eta_x n_z \hat{Y} + \eta_x n_y \hat{z}\right). \tag{C2}$$

We calculate the volume Ω about a single impurity containing nuclei with frequency shifts greater than some $\Delta\nu$.

The volume Ω is bounded by a revolution about the $\vec{\alpha}$ direction of a curve described by

$$r^2 = -\alpha\cos\phi/\Delta\nu \tag{C3}$$

where ϕ is the angle between $\vec{r}$ and $\vec{\alpha}$. For $\phi = 0$ there is a minimum frequency shift $\Delta\nu_0 = \alpha/r_0^2$ for the nuclei located on the crystal surface, a distance r_0 from the impurity. The maximum frequency shift is $\Delta\nu_m = \alpha/a^2$, for the nearest neighbor nuclei located at a distance a from the impurity. The volume within the nearest neighbor sites and outside the sample are excluded from Ω . These

exclusions eliminate unphysical infinities. The line shape will be shown to be independent of r_0 but not of a. Thus the sample dimension r_0 has no effect upon the line shape. Further, the near neighbor distance may be used to determine the location of the defect sites. The volume Ω is found by the simple integral

$$\Omega(\Delta\nu) = 4\pi\int_0^{\cos^{-1}(r_0^2\Delta\nu/a)}\sin\phi\,d\phi\int_0^{r_0}r^2dr + 4\pi\int_{\cos^{-1}(r_0^2\Delta\nu/a)}^{\pi/2}\sin\phi\,d\phi\int_0^{\sqrt{a\cos\phi/\Delta\nu}}r^2dr - \tag{C4}$$

$$-4\pi\int_0^{\cos^{-1}(a^2\Delta\nu/a)}\sin\phi\,d\phi\int_0^{a}r^2dr - 4\pi\int_{\cos^{-1}(a^2\Delta\nu/a)}^{\pi/2}\sin\phi\,d\phi\int_0^{\sqrt{a\cos\phi/\Delta\nu}}r^2dr\,.$$

The result is

$$\Omega(\Delta\nu) = \begin{cases} r_0^3\left(1-\frac{3}{5}\Delta\nu/\Delta\nu_0\right) - a^3\left(1-\frac{3}{5}\Delta\nu/\Delta\nu_m\right), & \Delta\nu < \Delta\nu_0\,, \\ \frac{2}{5}(a/\Delta\nu)^{3/2} - a^3\left(1-\frac{3}{5}\Delta\nu/\Delta\nu_m\right), & \Delta\nu_0 \le \Delta\nu \le \Delta\nu_m\,, \\ 0\,, & \Delta\nu_m < \Delta\nu\,. \end{cases} \tag{C5}$$

The number of nuclei $N_s(\Delta\nu)$ shifted by an amount greater than $\Delta\nu$ is $(3N/4\pi r_0^3)\Omega$, where N is the number of resonant nuclei in the sample. Then the distribution $g(\Delta\nu)$ of frequency shifts caused by a single impurity is

$$g(\Delta\nu) = -\frac{dN_s}{d\Delta\nu}\,. \tag{C6}$$

Combining Eqs. (C5) and (C6) the expression for $g(\Delta\nu)$ becomes

$$g(\Delta\nu) = \frac{3N}{5\Delta\nu_0}\begin{cases} 1-(\Delta\nu_0/\Delta\nu_m)^{5/2}, & \Delta\nu < \Delta\nu_0\,, \\ (\Delta\nu_0/\Delta\nu)^{5/2} - (\Delta\nu_0/\Delta\nu_m)^{5/2}, & \Delta\nu_0 \le \Delta\nu \le \Delta\nu_m\,, \\ 0\,, & \Delta\nu_m < \Delta\nu\,. \end{cases} \tag{C7}$$

Next the frequency shift distribution due to a number N_I of impurities randomly distributed throughout the sample must be calculated. Due to the long range nature of the induced efg, the satellite transitions of each nucleus are significantly affected by many defects, even at very low defect concentrations (10^{12} cm^{-3}). Thus one may use the central limit theorem[38] to calculate the frequency shift distribution due to a number N_I of randomly distributed defects. According to that theorem, the distribution will be gaussian with a second moment given by

$$\langle \Delta\nu^2 \rangle_Q = N_I \langle \Delta\nu_1^2 \rangle_Q$$

where $\langle \Delta\nu_1^2 \rangle_Q$ is the second moment of $g(\Delta\nu)$. Using the relation $\Delta\nu_0/\Delta\nu_m = a/r \ll 1$, one finds

$$\langle \Delta\nu^2 \rangle_Q = \frac{2\pi e^2 e^{*2} Q_I^2 R_{14}^2}{3a h^2 \epsilon^2} \rho_I f(\theta) \qquad (C8)$$

where θ is defined in Eq. (7), and ρ_I is the charged defect density.

Finally, the relation between the distribution of quadrupole frequency shifts $G_Q(\Delta\nu)$ (Basically an inhomogeneous broadening), and the NMR line shape $G(\nu)$ must be established. The quadrupole frequency shift distribution is a gaussian function with second moment $\langle \Delta\nu^2 \rangle_Q$.

$$G_Q(\Delta\nu) = \left(2\pi \langle \Delta\nu^2 \rangle_Q\right)^{-\frac{1}{2}} \exp\left(-\Delta\nu^2 / 2\langle \Delta\nu^2 \rangle_Q\right) \qquad (C9)$$

For the spin 3/2 case, the magnetic resonance line shape is found through the expression

$$G(\nu)=\int_{-\infty}^{\infty} d(\Delta\nu)\,G_Q(\Delta\nu)\left[.3G_{\frac{1}{2},\frac{3}{2}}(\nu-\Delta\nu,\Delta\nu)+.4G_{-\frac{1}{2},\frac{1}{2}}(\nu,\Delta\nu)+.3G_{-\frac{3}{2},-\frac{1}{2}}(\nu+\Delta\nu,\Delta\nu)\right] \quad (C10)$$

where $G_{1/2,\,3/2}(\nu-\Delta\nu,\Delta\nu)$ is the line shape function of the 3/2-1/2 transition caused by other broadening mechanisms (as modified by the quadrupole shifts). The first argument in the functional dependence of $G_{1/2,\,3/2}$ is the center frequency for the 1/2-3/2 transition and the second is intended to represent the effect the shift may cause on the line shape. The shape due to other interactions can be modified by the shifts, e.g.,terms in the dipolar hamiltonian that are secular in the absence of shifts will become non-secular when the shifts are large enough, thus modifying the width of the dipolar broadened line. $G_{-1/2,\,1/2}$ and $G_{-3/2,\,-1/2}$ are the corresponding shape functions for those transitions. The factors 0.3, 0.4, and 0.3 are weighting factors that arise from the transition matrix elements for the three transitions.

For the case of low defect concentrations treated here, we ignore the effect of the frequency shift upon the line shape. Further we assume that $G_{1/2,\,3/2}(\nu,0) = G_{-1/2,\,1/2}(\nu,0) = G_{-3/2,\,-1/2}(\nu,0) = G_0(\nu)$ where $G_0(\nu)$ is the lineshape in the absence of the quadrupole interaction. Then Eq.(C10), in view of these approximations becomes

$$G(\nu) = 0.4\,G_0(\nu) + 0.6\int_{-\infty}^{\infty} d(\Delta\nu)\,G_0(\nu+\Delta\nu)\,G_Q(\Delta\nu) \quad (C11)$$

If $G_0(\nu)$ is a gaussian with second moment $\langle \Delta\nu^2 \rangle_0$ then

$$G(\nu) = 0.6\left[2\pi\left(\langle \Delta\nu^2\rangle_0 + \langle \Delta\nu^2\rangle_Q\right)\right]^{-\frac{1}{2}} \exp\left[-\nu^2/2\left(\langle \Delta\nu^2\rangle_0 + \langle \Delta\nu^2\rangle_Q\right)\right] + 0.4\left[2\pi\langle \Delta\nu^2\rangle_0\right]^{-\frac{1}{2}} \exp\left[-\nu^2/2\langle \Delta\nu^2\rangle_0\right], \tag{C12}$$

where ν is centered at the Larmor frequency. Thus the second moment of the composite line is

$$\langle \Delta\nu^2 \rangle = \langle \Delta\nu^2\rangle_0 + 0.6\langle \Delta\nu^2\rangle_Q \tag{C13}$$

The Fourier transform of $G(\nu)$ is the FID function. Thus the quadrupole broadened FID should have the form of Eq. (19) with $I_1/I_2 = 2/3$ and $\alpha_2^2 = \alpha_1^2 + 4\pi^2\langle \Delta\nu^2\rangle_Q$.